Centrality Dependence of Two-Particle Correlations in Relativistic Heavy Ion Collisions

by

YOUNGSOO PARK

Submitted to the Department of Physics
in partial fulfillment of the requirements for the degree of

BACHELOR OF SCIENCE

at the

MASSACHUSETTS INSTITUTE OF TECHNOLOGY

June 2009

Author .....
Department of Physics
May 20, 2009

Certified by .....
Gunther Roland
Associate Professor of Physics
Thesis Supervisor

Accepted by .....
Professor David E. Pritchard
Senior Thesis Coordinator, Department of Physics

Centrality Dependence of Two-Particle Correlations in Relativistic Heavy Ion Collisions

by

YOUNGSOO PARK

Submitted to the Department of Physics
on May 20, 2009, in partial fulfillment of the
requirements for the degree of
BACHELOR OF SCIENCE

Abstract

Results on the centrality dependence of two-particle correlations in Au+Au collisions at $\sqrt{s_{\rm NN}} = 200$GeV are presented. A particular focus is devoted to investigating any anomalous behavior in the centrality dependence of correlation functions, as previous results suggest existence of such tendencies around $Npart \approx 50$.

Correlation functions are calculated for a wide kinematic region of $|\Delta\eta| < 3$ from data obtained by the PHOBOS experiment at RHIC. The RHIC layout and the PHOBOS detector setup is discussed. Data acquisition method employed by the PHOBOS experiment, data processing procedures and event selection criteria are presented. The two-particle correlation function is defined and calculation procedures are described. Decomposition analysis is explained as the fit function and the constituting components are introduced. Analysis results for correlation functions and fits are presented. The results suggest that in the kinematic region covered by the analysis of this thesis, no anomalous trends in component behavior exists.

Thesis Supervisor: Gunther Roland
Title: Associate Professor of Physics

To Soyoung, my Immortal Beloved.

Contents

1 Introduction

1.1 The Quest for Fundamental Particles and Forces

Human beings have always been fascinated by the idea of building blocks, since way before the first lego toys. Dating back to antiquity, abundant efforts were made to reveal the most basic constituents of the nature, as well as the way in which these building blocks interact with each other. As of today, it is believed that the Standard Model effectively describes all elementary particle needed to describe nature, with four fundamental forces creating various interactions between elementary particles or between structures formed by such particles.

The Standard Model constitutes of 12 flavors of elementary fermions known as quarks and leptons, categorized by three generations, with four elementary bosons acting as mediators for the four fundamental forces. All of these particles have been experimentally confirmed to satisfy the predictions of the Standard Model but one, the Higgs boson. A large portion of the Large Hadron Collider (LHC) experiment at European Organization for Nuclear Research (CERN) is now devoted to this final undiscovered particle, which, upon discovery, will complete the Standard Model understanding of nature.

The four fundamental forces constitute of gravity, electromagnetic force, weak force and strong force. Gravity, theorized the earliest among the four, is an attractive interaction between two massive bodies. It is the weakest among the four forces in terms of interaction strength but also the longest in terms of effective range. The next fundamental force to be understood was the electromagnetic force, which encompasses various interactions caused by the electric and magnetic fields. The electric force and the magnetic force was first understood separately, but was later unified by Maxwell in the 19th century. Weak force, placed between gravity and electromagnetic force on the interaction strength scale, is an extremely short-ranged force first discovered in radioactive decay phenomena. While it is weak in strength as its name suggests, it induces a range of interesting interactions through which

particles change flavor and fundamental symmetries of nature are broken. Strong force, strongest in strength among the four forces, is the attractive interaction that allows nuclei to hold together despite the electric repulsion between protons. In fact, strong force acts in a scale smaller than the nucleons, as it is explained by interactions between quarks and gluons that combine to form the nucleons.

While the elementary particles and forces are now clarified to a degree, the quest for a deeper understanding of nature is still very much ongoing. Various physics phenomena are not yet fully explained in terms of these basic understandings, and physics and physicists of today still pour that millennia-old effort to further the human knowledge of nature's underlying mechanisms. This thesis humbly places its roots at that very effort.

1.2 Quantum Chromodynamics and the QCD Phase Diagram

Quantum Chromodynamics (QCD) is the relativistic quantum field theory that explains the strong interaction between quarks and gluons. The pre-QCD model of quarks faced a roadblock when the doubly charged Δ^{++} baryon was discovered, as it required a configuration of three identical up quarks with equal spin states, which was not allowed in the naive quark model. To resolve this issue, QCD introduced the concept of a new charge, known as *color*. By introducing the three color charges of red, blue and green, it explained the colorless Δ^{++} baryon state as the configuration of three up quarks with the same spin states but of different color states. The concept of the color charge extends to gluons, the mediator of strong interactions described by QCD. QCD describes strong interaction by quarks exchanging eight massless gluon fields, where each of the eight gluons carry a color charge and an anticolor charge. Experimental results have later confirmed the existence of color as an inherent charge of quarks and gluons, supporting the validity of the QCD formulation.

An interesting result of QCD is a graphic description of its thermodynamic predictions, known as the QCD phase diagram, which shows different phases of matter at thermal equilibrium under various conditions. Study of thermodynamic properties is especially crucial in understanding phenomena at the parton level, and the current understanding of this phase diagram is shown in Fig. 1.1, displaying the different phases of QCD matter with respect to temperature T and baryon chemical potential

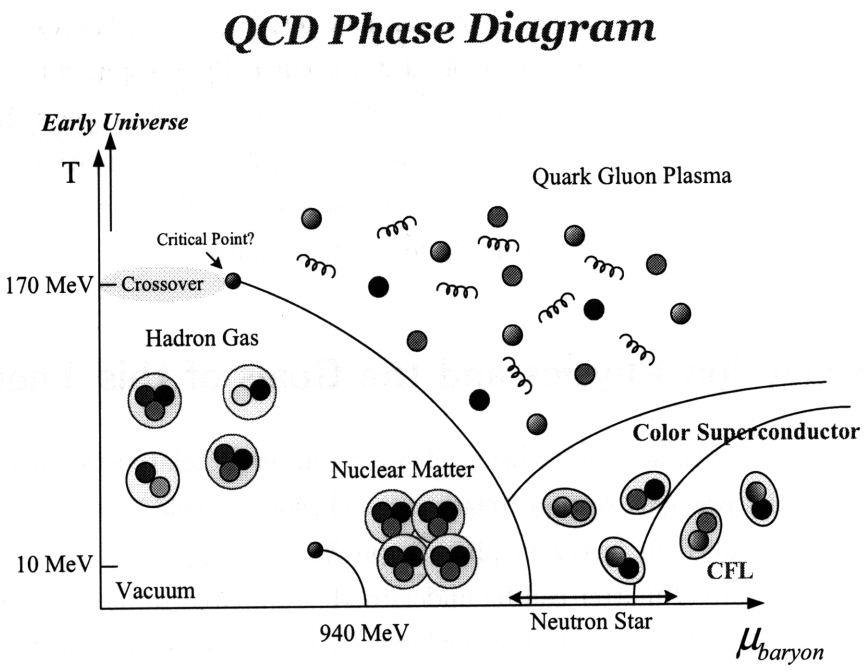

Figure 1.1: A schematic of the QCD phase diagram of nuclear matter in terms of the temperature (T) and baryon chemical potential (μ_B).

μ_B [1].

The ordinary nuclear matter phase is located at low temperature with μ_B around the mass of a nucleon ($\sim$ 940 MeV), where quarks and gluons are confined inside nucleons. This is the regime where the everyday forms of matter exist, as nucleons are bound into nuclei by strong interaction and atoms or molecules are formed. However, as μ_B decreases or temperature increases above the nuclear binding energy ($\sim$ 10 MeV), the nuclear matter dissolves and enters a "gaseous" state of individual hadrons, similar to the liquid-gas transition of the molecular matter [1].

1.3 The Quark-Gluon Plasma

An interesting phase in the QCD phase diagram is reached from the ordinary nuclear matter phase by raising temperature at constant (and low) baryon density. As the system is heated above the critical temperature T_c, quarks and gluons escape the nucleonic confinement and the system becomes a weakly interacting gas of quarks

[1]The chemical potential characterizes the amount of energy required to add another constituent into the system.

and gluons, known as the Quark Gluon Plasma (QGP) [2, 3]. The experimental success in production of the QGP state of matter is currently a disputed topic, but it is likely that it will be produced in heavy ion collisions at the LHC experiments. The exact nature of the interactions going on inside the QGP state of matter is not yet clarified, and a significant portion of particle physics, especially heavy ion physics, is now devoted to understanding this intriguing state of matter.

1.4 Heavy Ion Physics and the Goals of this Thesis

Heavy Ion Physics studies the collision of heavy nuclei at relativistic energies. As mentioned in the previous section, relativistic collisions of gold or copper nuclei, a common topic studied in heavy in physics, provides an important probe through which the QGP state of matter can be understood. Compared to p+p collisions, the "fireball" created at the moment of heavy ion collisions involves a far greater number of partons, which is a crucial requirement in forming a QGP-like state of matter. By studying the hadronization process immediately following this fireball state, clues about the nature of the QGP state may be gained. One example of such a clue is correlation between the hadronized particles emitted from the fireball, which provides direct insight into how the colliding partons must have interacted immediately before emission of such particles.

The analysis of this thesis involves the study of such correlations. In particular, this thesis focuses on the two-particle correlations observed in Au+Au collisions. Two-particle correlation is a measure of how likely the momentum directions of two randomly selected particles of a collision event satisfy certain constraints, e.g. similarly directed in a certain axis. It is now understood that these correlations constitute of different contributing components varying with respect to changing centrality. Therefore, this thesis attempts to decompose the overall effect of two-particle correlation into a set of expected components and study the behavior of each component separately.

Recent results from similar analyses carried out by the STAR collaboration [4] suggest that the component behavior shows anomalous trends as certain components exhibit rapid transitions in their magnitudes. More specifically, the strengths of angular correlation components, in addition to a component corresponding to minijet phenomena, show sudden increases around $N_{\text{part}} \approx 50$. The analysis of this thesis is based on data obtained by the PHOBOS experiment, and while the two experiments

derive from the same heavy ion collision events produced by RHIC, the characteristics of the two experiments widely differ in a number of aspects such as detector acceptance and multiplicity measurement capabilities. The strength of the PHOBOS detector, discussed in Sect. 2.2, is the wide acceptance range of its octagon detector, allowing this analysis to explore a far larger kinematic region of $|\Delta\eta| < 3$ compared to that of the STAR analysis ($|\Delta\eta| < 1$). Therefore, another goal of this thesis will be investigating whether this anomalous trend in component behavior can be confirmed in a wider kinematic range by studying the centrality dependence of two-particle correlations observed from Au+Au collision at $\sqrt{s_{\mathrm{NN}}} = 200\mathrm{GeV}$.

2 Experimental Setup

This thesis and its analysis makes use of data from the PHOBOS experiment of the Relativistic Heavy Ion Collider (RHIC), located at Brookhaven National Laboratory (BNL). As one of RHIC's four experiments, PHOBOS was designed to focus on the measurement of collision events in a global manner, made possible by the broad acceptance of its detectors. During its five-year run, PHOBOS measured p+p, d+Au, Cu+Cu, and Au+Au collision events at center-of-mass energies ranging up to $\sqrt{s_{\mathrm{NN}}} = 200\mathrm{GeV}$, yielding a sufficient amount of data for accurate studies of particle correlations. A list of current members and institutions at PHOBOS can be found in Appendix A. In this chapter, information on the design and characteristics of the PHOBOS experiment that is relevant to the analysis of this thesis is introduced.

2.1 Relativistic Heavy Ion Collider

The Relativistic Heavy Ion Collider (RHIC) [5, 6] at Brookhaven National Laboratory (BNL) was constructed to collide heavy ions in a variety of species (primarily Au^{+79}) over a wide range of energy (up to center-of-mass energy of 200 GeV per nucleon pair), including collisions between ions of unequal nucleon numbers (d+Au) and polarized protons. Four experiments were built to study these collisions, two bigger ones (STAR[1], PHENIX[2]) and two smaller ones (PHOBOS[3], BRAHMS[4]). The STAR detector [7] featured a large barrel Time Projection Chamber (TPC) which could identify the trajectories of almost all charged particles at mid-rapidity. The PHENIX detector [8], including two large muon hodoscopes, was designed specifically to measure direct probes of the collisions such as electrons, muons and photons. The BRAHMS experiment [9] was equipped with two movable spectrometer arms to

[1]Solenoidal Tracker At RHIC

[2]Pioneering High Energy Nuclear Experiment

[3]The original experiment MARS (Modular Array for RHIC Spectroscopy) was rejected. A smaller setup under the name of one of the moons of Mars was later built.

[4]Broad Range Hadron Magnetic Spectrometers Experiment at RHIC

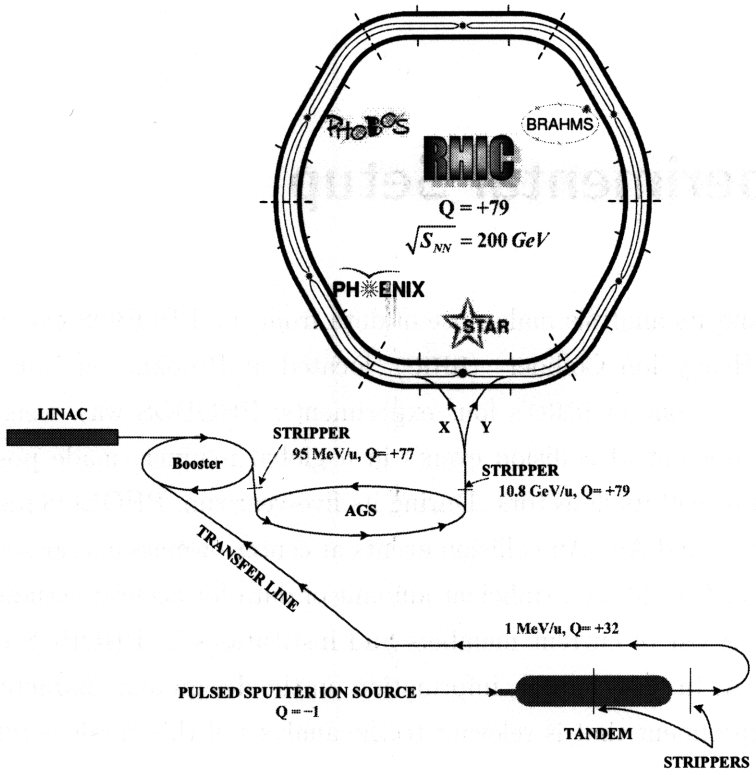

Figure 2.1: A schematic of the AGS-RHIC complex.

study identified particle production over a broad rapidity range, especially at the very forward region. The setups of the PHOBOS experiment are described in Sect. 2.2. The layout of the whole RHIC complex at BNL is displayed in Fig. 2.1.

2.1.1 Initial Stages and the AGS

The production of an initial beam of gold ions (Au^{+79}) starts at the Tandem Van de Graaff accelerator. Negative ions (Au^{-1}) produced by a pulsed cesium sputter ion source are accelerated to the high voltage terminal of the Van der Graaff with A 15 MV electrostatic field, stripping electrons from these ions through carbon stripper foils. Once the ions are in their +12 charge state, they enter another acceleration sequence now with a -15 MV electrostatic field, reaching energies up to 1 MeV per nucleon and ready to exit the Tandem. Additional stripper foils at the exit from the Tandem performs further stripping, and ions with a +32 charge state at the end of this sequence are selected magnetically to be transferred to the Booster synchrotron.

In the Booster synchrotron, further stripping of the remaining electrons in the

gold ions is performed. While the AGS, to be discussed later, possesses greater beam-focusing abilities, the Booster synchrotron is superior in the quality of the vacuum in use, allowing it to carry out the tasks of pre-acceleration and stripping without facing significant beam intensity loss due to interaction of the partially stripped ion beam with ambient gases. Upon exit from the synchrotron, the ions reach energies up to 95 MeV per nucleon, and those with a +77 charge state (i.e. only the K-shell electrons remaining) are then transferred to the AGS.

At the Alternating Gradient Synchrotron (AGS), the beam is focused in horizontal and vertical dimensions, resulting in a significant increase of the beam intensity. The key element of AGS in this maneuver is a set of alternating magnets with C-shaped tips. As the magnets alternate, the orientation of the magnetic field gradients also alternates inward and outward, resulting in a condensation of the dispersed ions inside the beam. This process and the subsequent acceleration of the beam ions provides acceleration to energies reaching 10.8 GeV per nucleon, and the accelerated beam is then finally transferred to the RHIC ring, during which it is stripped of the remaining two electrons to become a fully stripped Au^{+79} beam.

2.1.2 Relativistic Heavy Ion Collider Ring

RHIC collider ring system consists of two concentric quasi-circular superconducting storage-accelerator rings, referred to as blue and yellow rings, respectively. Each ring has six arc sections of length 356 m and six straight sections 277 m, with interaction points located in the middle of each straight section. Particles are directed and focused by superconducting dipole and quadrupole magnets, maintained at temperatures below 4.2 K by liquid helium cooling. The dipole magnet provides a uniform magnetic field of 3.458 T in the arc sections of the ring to appropriately bend the beam along the ring circumference, while the quadrupole magnets keep the beam focused. At each interaction point, two DX and D0 magnets are located on the entering and exiting sites, where the D0 magnets guide the two separate beams in the blue and yellow rings to a single beam pipe and the DX magnets steer them to collision.

Each bunch crossing involves $\sim 10^9$ nuclei. The bunches are first captured in stationary buckets, and are transferred to the storage system after reaching the target beam energy. This storage procedure constrains the bunch length ($\sigma_L \approx 25$ cm) by reducing intrabeam scattering. When two filled buckets collide at an intersection point, the RHIC "crossing clock" informs the experiments of the time and location of the collision. In general, the beam luminosity is in the 10^{26} - 10^{27} $cm^{-2}s^{-1}$ range for

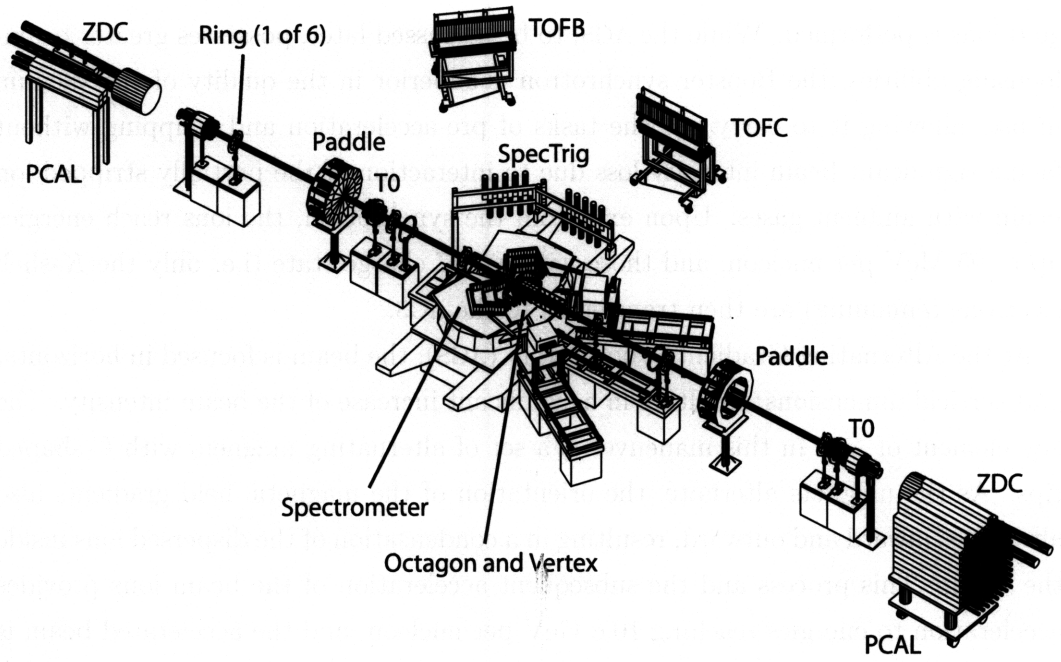

Figure 2.2: The complete PHOBOS detector setup.

the heaviest ions.

2.2 PHOBOS Detector Setup

As previously discussed, the PHOBOS detector has its primary focus in the global measurement of the collision events, and its design allows it to successfully achieve this goal. A central multiplicity silicon array with full 4π coverage of the azimuthal angle detects nearly all outgoing particles produced in a collision event. A mid-rapidity two-arm Spectrometer, serving as the tracker, allows full reconstruction of particle trajectories for about 2% of all outgoing particles. In addition, a set of detectors at forward regions allows particle detection over a wide range of rapidity, enabling effective event triggering and accurate centrality determination. A diagram of the complete PHOBOS setup is shown in Fig. 2.2.

2.2.1 Multiplicity Array

The PHOBOS central multiplicity array consists of a barrel Octagon detector covering pseudorapidity range $|\eta| < 3.2$ with nearly full azimuthal coverage and two sets of three Ring counters perpendicular to the beam axis that extend to pseudorapidty

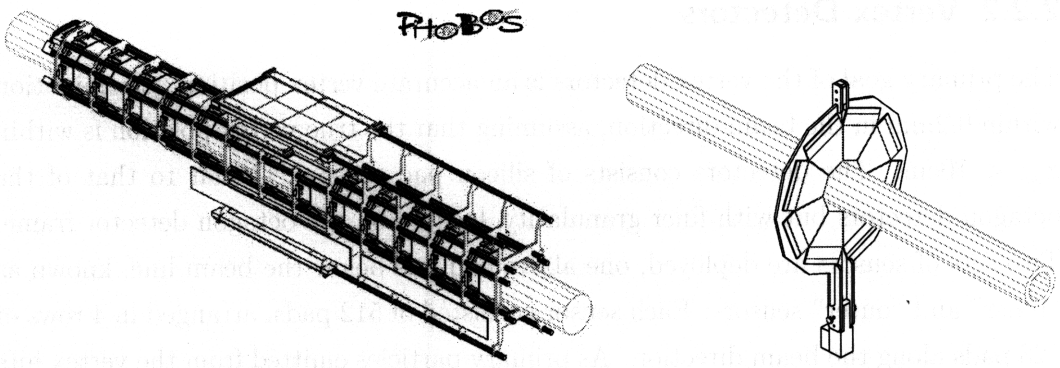

(a) Octagon and Vertex Detectors (b) Ring Detector

Figure 2.3: The PHOBOS multiplicity detectors [10].

range $|\eta| < 5.4$. The energy deposited by the charged particles are measured by these two detectors.

Octagon Detector

A schematic of the octagon detector, consisting of 92 silicon pad sensors, is shown in the below Fig. 2.3 [10]. Its name derives from a 1.1 m long, 9 mm diameter frame with eight faces, upon which the pads were attached. Each sensor was 84 mm long and 36 mm wide with a thickness of approximately 300 μm, which contains 120 subsections, or pads, arranged in 4 rows of 30 pads parallel to the beam direction. With more than 95% of its sensors active with a signal-to-noise ratio above $S/N \approx 12/1$, the octagon detectors obtained trustworthy data crucial for the analysis of this paper.

Ring Detectors

Particles outside the pseudorapidty range of the octagon detectors are measured by the ring detectors, also shown in Fig. 2.3(b) [10]. Six ring detectors are deployed in the PHOBOS experiment, placed ± 1.13 m, ± 2.35 m and ± 5.05 m away from the interaction point, corresponding to pseudorapidity ranges of $3 \leq |\eta| \leq 4$, $4 \leq |\eta| \leq 4.7$ and $4.7 \leq |\eta| \leq 5.4$, respectively. Each ring detector consists of eight trapezoidal silicon sensors, each containing 64 pads arranged in 8 rows and 8 radial columns. Sizes of the pads were varied for approximately equal pseudorapidity coverage ($\Delta\eta \approx 0.1$) throughout all pads, assuming vertex location of $z_{vtx} = 0$. Ring detectors has a similar signal-to-noise ratio to that achieved by the octagon detectors.

2.2.2 Vertex Detectors

The primary goal of the vertex detectors is an accurate vertex position determination within 0.2mm in the beam direction, assuming that the true vertex position is within $z_{vtx} < 10$cm. The detectors consists of silicon pad sensors, similar to that of the octagon detectors but with finer granularity, located on the octagon detector frame. Two sets of sensors are deployed, one above and one below the beam line, known as "inner" and "outer" sensors. Each sensor consisted of 512 pads, arranged in 4 rows of 128 pads along the beam direction. As primary particles emitted from the vertex hits the two layers, a set of two-point tracklets can be obtained, and the vertex position can be determined by finding the intersection of all meaningful tracklets. The upper 4 x 2 array of the Outer Vertex sensors can be seen in Fig. 2.3 [10].

2.2.3 Spectrometer Detectors

Spectrometers serve as the main tracker detectors for the PHOBOS experiment, providing full track reconstruction for nearly 2% of all outgoing particles. The two spectrometer arms are situated in a 2 T magnetic field, and particle momenta are determined from the curvature of the particle's trajectory inside the magnetic field. A Time-of-Flight (TOF) wall is installed further away from the beam pipe to obtain the velocity of the particles, and momenta of particles in the lower momentum range that could not penetrate the whole spectrometer array can still be determined from the energy loss obtained from the silicon detectors. Each of the two arms has 137 sensors and 780 readout chips assembled into 42 multi-sensor modules, adding up to a total of 56,064 channels. The overall configuration of the spectrometer is shown in Fig. 2.4 [11].

2.2.4 Triggering System

The PHOBOS triggering system consists of the following three main components:

- The Paddle counters for Minimum Bias (MinBias) event triggering in high multiplicity Au+Au collisions;
- The Time-Zero Counters (T0s) for vertex positioning
- The Zero-Degree Calorimeter (ZDC) as an experiment independent event trigger.

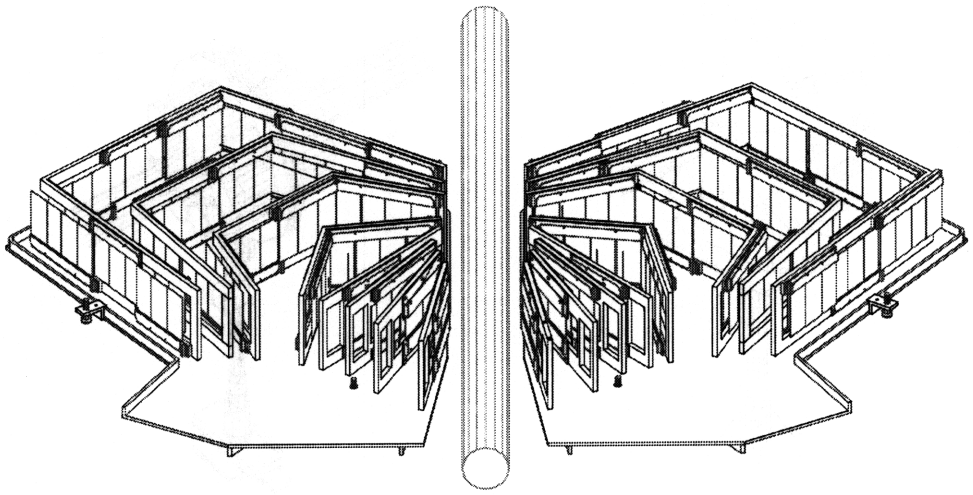

Figure 2.4: The PHOBOS spectrometer detectors. [11].

Additionally, the Spectrometer Trigger (SpecTrig) counters were installed between TOF wall and the Spectrometers right before 2003 d+Au run, in order to access more events with high p_T particles. There were Čerenkov counters, two sets of 16 Lucite radiators arranged around the beam pipe at ±5.5 m. However, they were replaced by the T0s with much better precision and no longer used after the d+Au run.

Paddle Counters

Under high multiplicity conditions such as in Au+Au collision events of this paper's interest, the paddle counters located at the forward ends of the detector are the most useful in triggering. Each counter consists of paddle-shaped plastic scintillators, each made of two planar arrays of 16 wedge-shaped scintillators, extending through a pseudorapidity range of $3 < |\eta| < 4.5$ with more than 99% of its scintillators active. Each scintillator is a 18.6 cm long, 0.95 cm thick plastic structure with varying widths. Triggering is carried out by counting the number of scintillators fired and the energy deposited upon the scintillator, and a trigger efficiency of 100% from semi-peripheral to most central event was achieved, providing a perfectly unbiased event trigger on all collisions. A diagram of a paddle counter is shown in Fig. 2.5(a).

Time-Zero Counters

The Time-Zero Counter (T0) replaced the original Čerenkov counters in order to provide more precise start-time measurement for the TOF, as well as real-time vertex

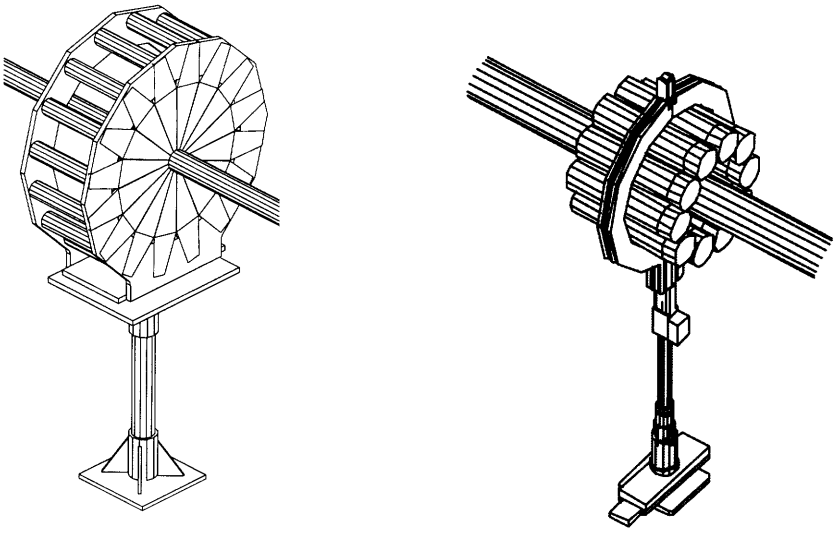

(a) Paddle Counter (b) Time-Zero Counter (T0)

Figure 2.5: Schematic diagrams of trigger counters: (a) Paddle Counter [12] and (b) Time-Zero Counter (T0).

information used in event triggering. There are two T0s, each consisting of 10 modules arranged in a circle of 151 mm in diameter about the beam pipe. They are located 5.4 m away from the interaction point but the distance was variable with respect to the type of collision events in measurement. The original Čerenkov counters had a rise time twice slower than the T0s counters, and the replacement resulted in a significantly improved timing resolution of 110 ps. A diagram of one T0 Counter is shown in Fig. 2.5(b).

2.2.5 PHOBOS Computing Architecture

PHOBOS computing is done through the RHIC Computing Facility (RCF) [13]. Raw data are first collected on a High Performance Storage System (HPSS) tape storage system, and processing or event reconstruction on this raw data is done through a distributed storage farm. For PHOBOS, the raw data are transferred from the HPSS onto the distributed computing farm, as detector simulation and physics analysis work are carried out on a separate computing cluster consisting of hundreds of computers through the Condor parallel processing system.

Data processing and analysis is done through the PHOBOS Analysis Toolkit (PhAT) software, based on the ROOT [14] object-oriented C++ framework. PhAT

consists of PHOBOS-specialized classes and macros, and allowed efficient handling of the large data from the heavy ion collision events based on the `TTree` data structure provided ROOT. PhAT's own analysis framework, known as the Tree-Analysis Modules (TAM), serves as the the main tool for data processing and analysis, through a hierarchy of submodules.

3 Calibration and Data Acquisition

The raw signals obtained from collision events must go through calibration and correction procedures to be used as proper data for event reconstruction and analysis. In this chapter, the processes of data readout, data acquisition, noise and gain calibrations and online/offline event selection procedures are discussed.

3.1 Readout

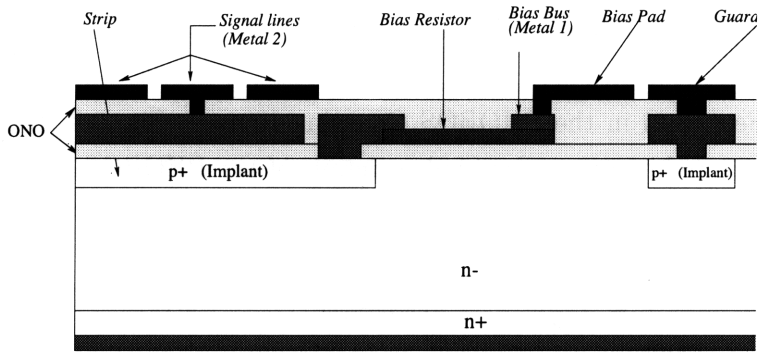

Figure 3.1: Schematic of a typical PHOBOS silicon detector. [15].

Schematics for different types of silicon detectors discussed above are shown in Fig. 3.1. All of these detectors uses VA-HDR-1 chips (64- or 128- channel version depending on the sensor granularity) as the readout, manufactured by the IDEAS company (http://www.ideas.no) . The chips are mounted on a hybrid with chip inputs directly wire-bonded to the sensors, as shown in Fig. 3.2. The initial signal read by the chips are first pre-amplified and then digitized by 12-bit Analog-to-Digital Converters (ADCs) in the Front-End Controllers (FECs). Them, digitized signals from each FEC are sent to the Data Multiplexing Unit (DMU) in the Data Concentrator, where they are again transmitted over optical fibers to the Data Acquisition (DAQ)

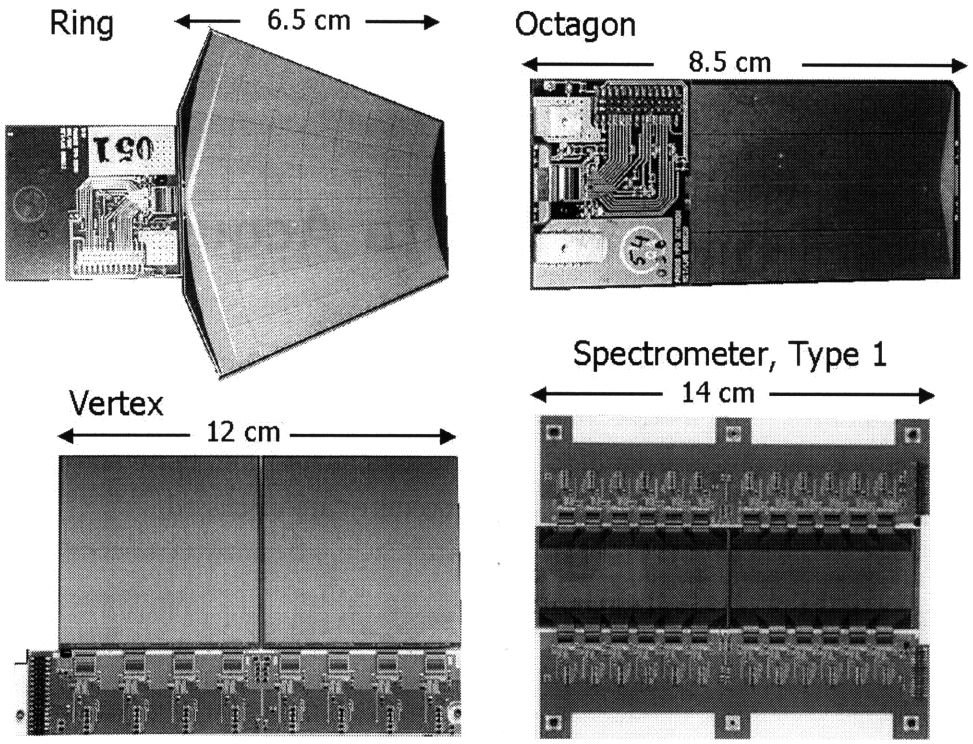

Figure 3.2: Photographs of four types of silicon sensor module.

system (see Sect. 3.2) in the PHOBOS Counting House. Fig. 3.3 [16] summarizes the full readout architecture. For further details of the PHOBOS detector readout, see Ref. [16].

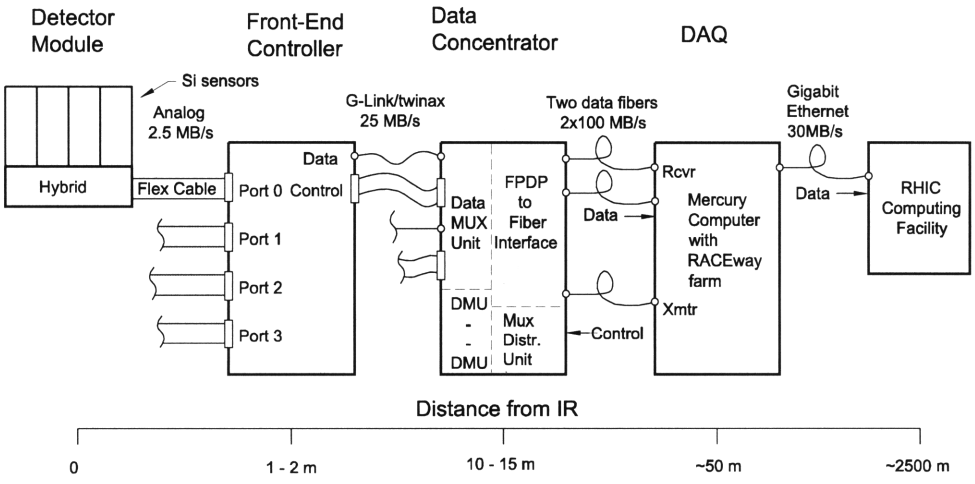

Figure 3.3: Schematic of the PHOBOS silicon detector readout architecture. [16].

3.2 Data Acquisition

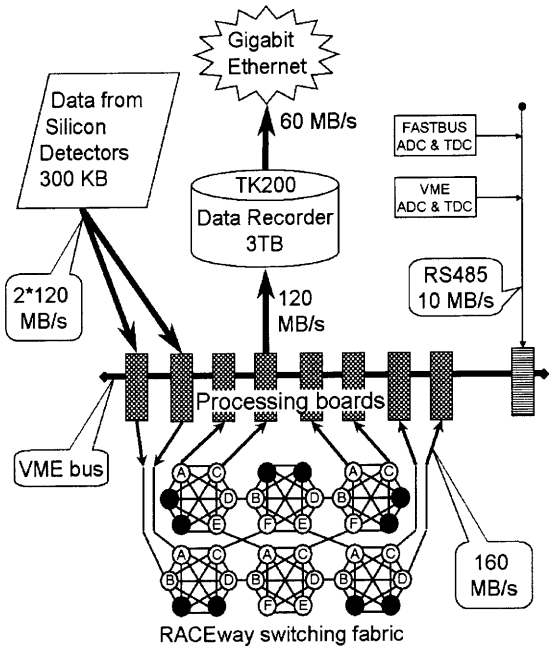

Figure 3.4: Schematic of the PHOBOS Data Acquisition (DAQ) system [17].

The PHOBOS Data Acquisition (DAQ) system achieved an event processing rate over 200 Hz while taking data from 135,000 silicon and 1500 scintillation detector channels. The obtained data were sent to the RHIC data storage at a rate of 30 Mb/s. The system consists of 24 300 MHz PowerPC-750 CPU farm, an event builder, temporary data storage, trigger monitor and a server, all housed in a VERSAmodule Eurocard (VME) crate. The various parts of the PHOBOS DAQ system are shown in Fig. 3.4 [17].

Once data is received, decision is made whether to record it to disk or not from trigger detector signals. Details of various triggering algorithms are described in Sect. 3.5. A large section of the system is devoted to perform Common-Mode Noise (CMN) corrections and zero suppression, discussed in Sect. 3.3, as well as data compression. Once the signals from the silicon detectors are combined with those from the scintil-

lators, the data is sent to the event builder through a Front Panel Data Port (FPDP) connection at a rate of 43 MB/s. The event is then stored in memory until it could be written to the disk cache. The event builder produces sequences of about 10,000 events, where each event is stored in ROOT file format with sizes roughly about 1 Gb. The event data are then transferred to the High Performance Storage System (HPSS) at RHIC over a Gigabit Ethernet connection.

3.3 Noise and Energy Calibrations

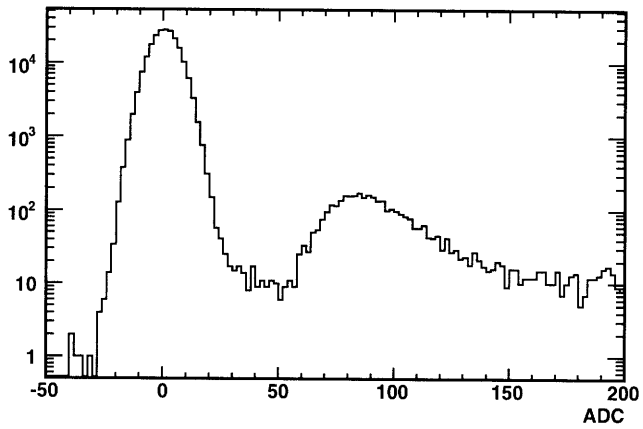

Figure 3.5: A typical ADC signal after Pedestal correction. [18]. Notice that the width of the peak centered at zero represents the noise fluctuation.

Pedestal and Random Noise Corrections

The silicon detectors in use at the PHOBOS experiment produces a characteristic noise known as a "pedestal" noise. Caused by leakage currents in the electronics, this noise creates a baseline signal in the ADC that becomes particularly dominant in low-multiplicity events where all silicon pads may not be hit by a particle. Therefore, appropriate suppressions must be performed to the raw signal to eliminate this effect. To determine the appropriate level of suppression, a pre-pedestal signal is established from the average of the first few hundred events of a run. Then, a second set of events were processed to locate a peak in energy distribution compared to the pre-pedestal, which determines the average value of the pedestal noise. Finally, a gaussian is fit to this peak to obtain the amplitude of noise fluctuation.

Besides the pedestal noise, a random fluctuation in the bias voltage applied to a sensor causes subsequent random errors in signals from all pads belonging to that sensor, known as the Common-Mode Noise (CMN). To correct for CMN, signals first corrected for pedestal noise are examined event-by-event, where each channel was investigated for any offset the pedestal-subtracted signals were collected for groups of channels event-by-event. A non-zero offset is then considered as CMN and was subtracted.

Energy Calibration

Energy calibration refers to the process of converting raw ADC signal to the actual energy deposit signal. In this process, reference signals known as Digital-to-Analog Converter (DAC) signals are first fed into the detectors. The raw signal from this reference input is digitized by the front-end amplifiers, and the resulting ADC signals are calibrated to the input signal. Results show that one unit of ADC signal corresponds to 2.1 keV of energy deposit, which translates to about 80 keV of the original hit energy. The calibrated signal is further suppressed for hits with very low energies, where a significant number of hits are discarded. This process achieves the twin goals of further removal of the pedestal noise discussed above, as well as reduction in event data size.

3.4 Dead and Hot Channel Corrections

Detector channels can malfunction in two ways: one, referred to as "dead", which implies that the channel does not transmit a signal even if it is hit, and two, referred to as "hot", which implies that the channel exhibits unreasonably many hits or hits with energies too high. To remove the incorrect data coming from these channels, a baseline is established by averaging the number of hits and energy of each hit for all silicon channels over many events. Then, individual channels are examined to see if their signals are significantly different from the baseline, either positively or negatively, and those who are determined to be either dead or hot are disregarded in the data-taking procedure. A map of the dead (red) and hot (green) channels in the octagon detector, accounting for about 8% of all channels, is illustrated in Fig. 3.6. Details of dead/hot channel determination can be found in Ref. [18].

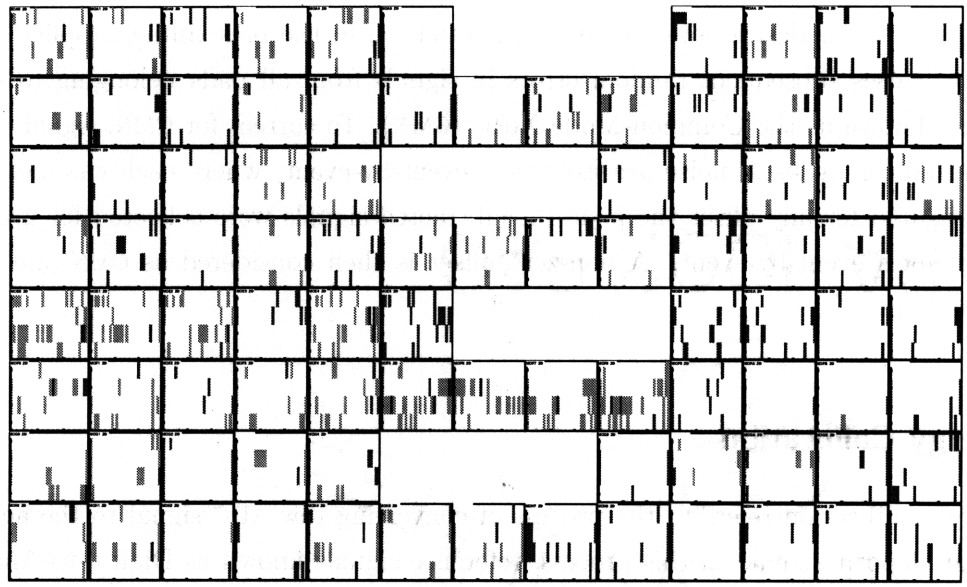

Figure 3.6: Dead(red) and hot(green) channel distribution in the octagon detector.

3.5 Online Event Selection

In analyzing heavy ion collision events, event selection is an essential part of any experiment. Since nucleons interact only within very short distances, a beam crossing does not necessarily mean a meaningful collision event, and in fact there is a significant difference between the beam crossing rate and the event rate. Therefore, for each beam crossing event a decision must be made on whether the event contains meaningful physical content, and whether the data gathered from that event will be stored or discarded. This decision is made by event triggering, an algorithm that rapidly determines the nature of an event from important indicators. There is a way of skipping this step, known as the Zero-Bias triggering method, where the crossing-clock of the RHIC accelerator is used to store whatever data recorded at the times that the beams are known to have crossed each other. However, most Zero-Bias events are beam-gas interactions, which contains little physics content of our interest. As discussed above, the PHOBOS experiment makes use of paddle and T0 counters to obtain the main triggering information. A range of trigger settings [19] are employed over the course of data-taking, and this section describes the ones relevant to the analysis of this paper.

3.5.1 The Minimum Bias Trigger

The MinBias trigger, as is apparent from its name, attempts to generate as few discarded events as possible, consequently creating a minimum of statistical bias through triggering as well as event loss. The PHOBOS experiment uses its paddle counters from MinBias triggering as it requires at least one scintillator array, or paddle, to be fired in both the positive and the negative side. The large acceptance and excellent trigger efficiency of the paddle counters make it ideal for triggering even on the low-multiplicity side, e.g. for p+p collisions. A slightly modified trigger criteria are employed for higher multiplicty events such as the Au+Au events analyzed in this paper, as at least two paddles were required to fire in each counter. For the high-multiplicity events, however, there was room for more selective triggering to be performed, and the majority of events were selected under the vertex trigger.

3.5.2 The Vertex Trigger

Vertex trigger is based on the idea of selecting events that has its primary vertex within a close range to the center of the detector, i.e. $|z_{vtx}| < 10$ cm. While the MinBias trigger makes use of the paddle counters, vertex trigger utilizes the T0 counters to exploit an order-of-magnitude advantage in timing resolution. The triggering criteria are based on the time difference of signals recorded in the T0 counters at both sides of the beam path, as the signal arriving at the T0 counter closer to the vertex would be measured slightly faster than the signal arriving at the further side. In addition to the T0 counters, ZDC information is used to sort out beam-gas interaction events during theAu+Auruns, as an additional requirement of simultaneous energy deposit at both ZDCs, ensuring the occurrence of a heavy ion collision, is incorporated into the trigger criteria.

3.6 Offline Event Selection

On top of the online event selection procedures, an addition set of offline event selection utilizing secondary trigger information is performed to get rid of leftover beam-gas events and flag events with meaningful physics contents for analysis.

3.6.1 p+p Event Selection

For reference p+p event selection, Non-Sigle-Diffractive (NSD) events are chosen by requiring both arms of the paddle counters to have at least one scintillator, or paddle, to be fired. The offline event selection for p+p events are carried out for events with MinBias trigger, and, since the T0 counters cannot be used for p+p triggering due to its small acceptance, a procedure similar to vertex triggering was implemented with the substitute variable Paddle Time Difference (PdlTDiff).

3.6.2 Au+Au Event Selection

Offline event selections in Au+Au collisions includes a cut on PdlTDiff as well as a requirement on the ZDC timing, mainly to reject beam-gas events. For beam-gas events occurring outside the region between the two paddle counters, the time difference in the two paddle counter signals is significantly large to be used as a selection criteria, and a cut of ± 4 ns on PdlTDiff was implemented to rule out such events. As for beam-gas events inside this paddle-to-paddle region, the fact that presence of only one beam direction inside the event causes an overall directionality in particle production is exploited. More specifically, since spectators neutrons will only reach one of the two ZDCs in beam-gas events, i.e. the one facing the beam direction, requiring that both ZDCs obtain a significant energy deposit successfully rules out these events. However, this requirement is overridden in the most central events, as this type of events will leave little to no spectator neutrons to reach the ZDC detectors. Such cases are determined by large signals in both paddle counters, where events satisfying this criterion was relieved of the ZDC coincidence requirement.

4 Analysis Methods

The analysis of this paper has its main goal in determining how the different components contributing to two-particle correlation behaves with respect to changing centrality, thereby revealing how the underlying physics effects combine with each other to produce the observed two-particle correlation. To achieve this goal, three crucial steps must be taken. One, the centrality of an event must be accurately determined so that the event may be classified with other events of similar centralities. Two, an appropriate measure of two-particle correlation, known as the correlation function, must be calculated for each event. Three, the resultant correlation function must be fit with a fit function constituting of the sum of various contributing components, and the behavior of the fit parameters must be extracted. This chapter is devoted to describing this analysis procedure in detail.

4.1 Centrality Determination

Centrality is a measure of how head-on the two bunches of beam particles crossed each other in a collision event. Best represented by the impact parameter b of the collision geometry, it is one of the most important initial conditions to be considered in heavy ion collisions. Centrality determination is a complex yet crucial element in studying collision events. It is complex in that the impact parameter is not an experimental observable, thereby requiring accurate estimations through means of relevant centrality-dependent indicators. Also, it is crucial in that the initial geometry of an event is a major determinant of the physics phenomena contained by that event. There is a vast difference between the physics contents of a central event and that of a peripheral event, meaning that correct estimation of centrality leads to correct understanding of the underlying physics. For the purposes of this paper, centrality determination gains an additional significance as it is required to successfully analyze behavior of two-particle correlations over different ranges of centrality.

In PHOBOS, centrality is determined by estimating the fractional cross-section of

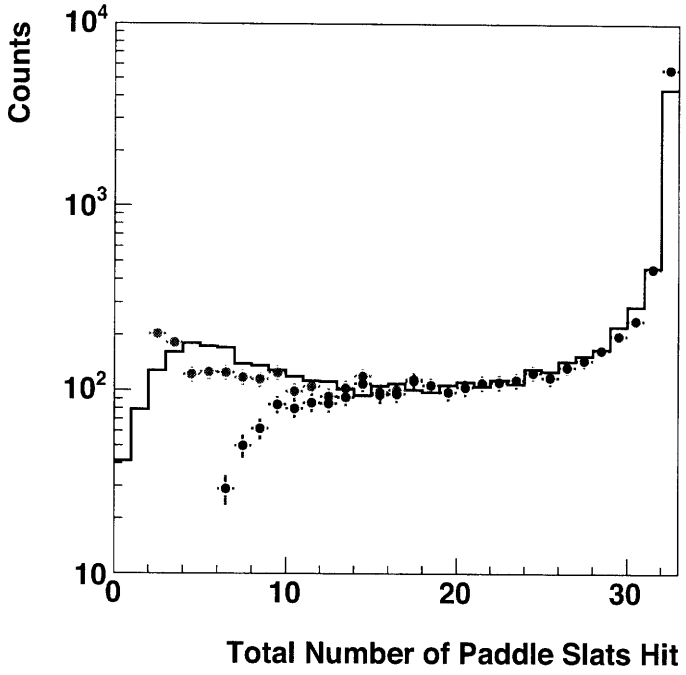

Figure 4.1: Distribution of paddle hits for HIJING (black line), Au+Au with n¿0 requirement (red points), Au+Auwith n¿2 requirement (blue points).

a collision from multiplicity measurements.

The centrality classification procedure at PHOBOS generally followed three basic steps:

- Comparing data and MC to correct for trigger efficiency, especially for low-multiplicty events;
- Dividing the distribution of a multiplicity variable into bins of fractional cross-section;
- Relating the fractional cross-section bins to centrality variables via Glauber model.

A more detailed description of centrality determination procedures is presented in [19].

4.1.1 Trigger Efficiency Correction

In using fractional cross-section bins as centrality determinants, it is crucial that a uniform yield of events is achieved over all centralities. Using uncorrected event data does not achieve this uniform yield, mainly due to the fact that trigger efficiencies are

higher for high-multiplicity events compared to low-multiplicity events. Therefore, this effect must be corrected for in order to give a proper account of events with both low and high multiplicities. To do so, the number of fired paddles in an event is compared between real events and HIJING, as shown in Fig. 4.1. Paddle hits are chosen not only because they are event triggers, but also due to the fact that number of paddle hits rises with event multiplicity. A plateau was identified to extend from 15 to 22 hits, and the rest of the 0-to-32 range was normalized to this plateau. Then, the trigger efficiency is defined as the ratio of all events in data to the sum of data events with high multiplicity (16 to 32 hits) and Monte Carlo (MC) events with low multiplicty (0 to 15 hits), as below.

$$\epsilon = \frac{N_{slat}^{Data}(0, 32)}{N_{slat}^{MC}(0, 15) + N_{slat}^{Data}(16, 32)} \tag{4.1}$$

This process removes the possibility of HIJING deviating from data in high-multiplicitiy, and therefore high-centrality, events, while applying the trigger efficiency corrections for low-multiplicity events.

4.1.2 Fractional Cross-section Binning

With the correct trigger efficiencies, events are first sorted by a multiplicity variable dependent on centrality, in our case the mean of the energy in the paddles (Paddle Mean (PdlMean)). The relationship between PdlMean and centrality, represented by N_{part}, is shown in Fig. 4.2(a). While the dependence may not be completely linear, monotonocity suffices for fractional binning. Once sorted by PdlMean, events are divided into 18 fractional cross-sectional bins, where the number of events in each bin, when corrected for trigger efficiency, is the same.

4.1.3 Centrality Variables

The last step in centrality determination involves attributing relevant centrality variables, such as N_{part} and N_{coll}, to the fractional cross-section bins. It was noticed that HIJING and data exhibits extremely similar paddle hit distribution, as shown in Fig. 4.1. Since HIJING takes N_{part}, and even the impact parameter b, as initial conditions, the N_{part} distribution of each bin was estimated from the corresponding HIJING distribution, as shown in Fig. 4.2(c). For each bin, the mean N_{part} value is calculated from the respective N_{part} distributions, and this value is taken to be the

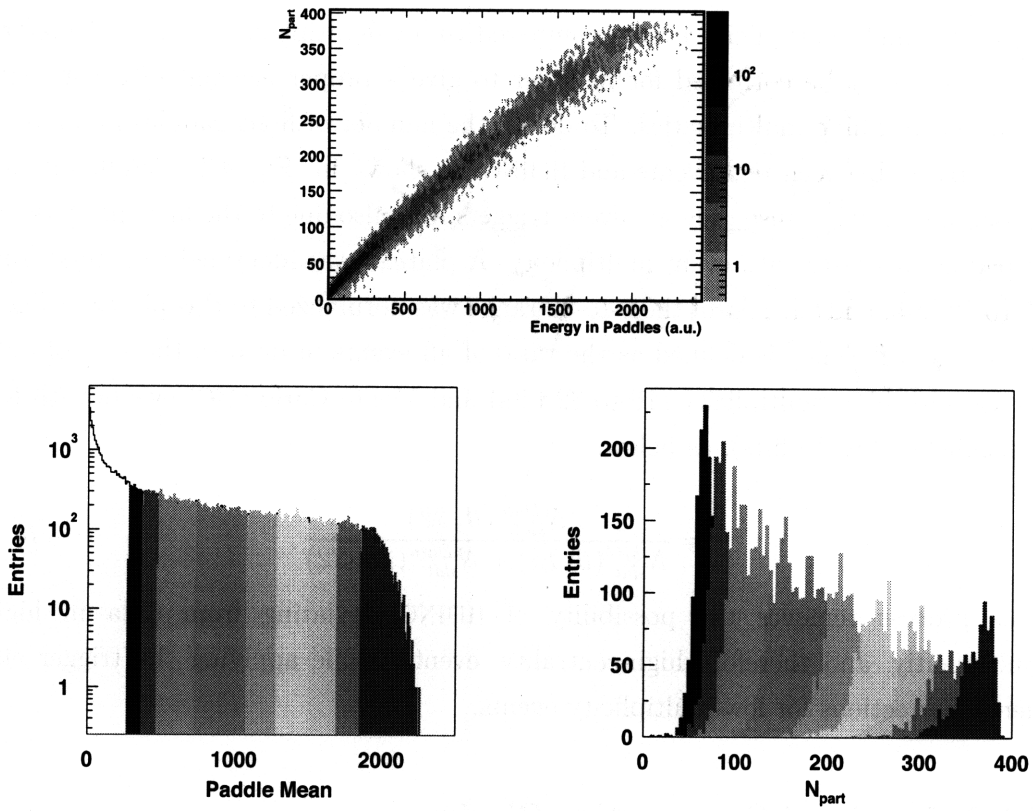

Figure 4.2: (a) PdlMean versus N_{part} distribution from HIJING simulation. (b) Color-coded fractional cross-sectional bins spanned by PdlMean. (c) Color-coded fractional cross-sectional bins spanned by $N_{\text{part}}$from MC results. Figures are taken from Ref. [18].

representative N_{part} value related to that bin. As for N_{coll}, a Glauber model calculation [20] is used. See Appendix C for the description of the Glauber model. The resulting centrality binning information is presented in Appendix D

4.2 Two-particle Correlation Function

Two-particle correlation functions describe the increased probability of two particles inside a collision event satisfying a set of constraints, in our case the difference pseudorapidity and azimuthal angle between the two momentum directions of the respective particles. The raw probability of two particles satisfying such constraints will not provide interesting results, due to the fact that it will be dominated by combinatorial effects. Rather, in order to inspect the effect of correlation on this

probability, we need to compare the probability of uncorrelated particle pairs satisfying the constraints with that of correlated particle pairs. The former is commonly known as the *background* of a correlation function, while the latter is referred to as the *signal*.

To formulate a rigorous definition for correlation functions, we follow an approach similar to that in Ref. [21]. Recognize that the aforementioned probability distribution is a particle-pair density distribution in the $(\eta_1, \eta_2, \phi_1, \phi_2)$ space, where the parameters denote the pseudorapidity and the azimuthal angle of momentum directions carried by the respective particles. The particle-pair density distribution ρ_n^{II}, serving as the signal, will be defined as following:

$$\rho_n^{\mathrm{II}}(\eta_1, \eta_2, \phi_1, \phi_2) = \frac{1}{n(n-1)\sigma_n} \frac{d^4\sigma_n}{d\eta_1 d\eta_2 d\phi_1 d\phi_2}, \tag{4.2}$$

where σ_n is the total cross section of observing events with n charged particles. Furthermore, to establish the background, we first define the single-particle density distributions as following:

$$\rho_n^{\mathrm{I}}(\eta, \phi) = \frac{1}{n\sigma_n} \frac{d^2\sigma_n}{d\eta d\phi}. \tag{4.3}$$

From this definition, the background particle-pair density distribution can be defined as

$$\rho_n^{\mathrm{I}}(\eta_1, \phi_1)\rho_n^{\mathrm{I}}(\eta_2, \phi_2). \tag{4.4}$$

The correlation function derives from the ratio of the signal to the background. Any deviation of this ratio from unity implies correlative effects. Therefore, the correlation function may now be defined as

$$R(\eta_1, \eta_2, \phi_1, \phi_2) = \left\langle (n-1) \left(\frac{\rho_n^{\mathrm{II}}(\eta_1, \eta_2, \phi_1, \phi_2)}{\rho_n^{\mathrm{I}}(\eta_1, \phi_1)\rho_n^{\mathrm{I}}(\eta_2, \phi_2)} - 1 \right) \right\rangle. \tag{4.5}$$

Notice that the resulting correlation function is defined in a four-dimensional space. It is not only difficult to visualize such a function, but also more intuitive results can be obtained by reducing the parameter space to a two-dimensional $(\Delta\eta - \Delta\phi)$ space, where $\Delta\eta = \eta_1 - \eta_2$ and $\Delta\phi = \phi_1 - \phi_2$. Then, a two-dimensional correlation function can be defined as

$$R(\Delta\eta, \Delta\phi) = \left\langle (n-1) \left(\frac{\rho_n^{\mathrm{II}}(\Delta\eta, \Delta\phi)}{\rho^{\mathrm{uncorr}}(\Delta\eta, \Delta\phi)} - 1 \right) \right\rangle. \tag{4.6}$$

In the analysis of this paper, the spatial extent of the octagon detector limit the range of the parameters of the particle-pair density distribution, and a corresponding limit is applied to the single-particle density distributions, specifically $-3 < (\eta_1 + \eta_2)/2 < 3$

and $-180° < (\phi_1 + \phi_2)/2 < 180°$. This then limits the range of the newly defined parameters as $|\Delta\eta| < 6$ and $|\Delta\phi| < 180°$.

The actual business of calculating this correlation function is a separate matter from the mathematical definitions. The signal can be calculated by taking all possible particle pairs in an event, constructing a histogram by filling it with their $\Delta\eta$ and $\Delta\phi$ values, and normalizing to unity integral. However, since an uncorrelated particle-pair distribution cannot be obtained within a single event, the technique of event-mixing must be used in obtaining the background. In event-mixing, a particle pair is constructed with two particles from two different events, thereby reproducing the convolution of two single-particle density distributions discussed above. To minimize statistical bias, the two events from which the particle pair will be constructed would be selected randomly. However, since event characteristics such as multiplicity differs with event centrality and vertex position, the selection range is constrained to be within the same centrality bin as the signal and to have a vertex position difference within 0.2 cm.

A set of sample signal and background distributions, drawn from from PYTHIA-generated events, are shown in Fig. 4.3. We notice that while the raw signal and background reveal little information about how correlation affects the particle-pair density distribution, the calculated correlation function effectively shows various structures arising from correlation effects. These structures will be discussed in detail in the following sections.

4.3 Systematic Uncertainties

The correlation function carries an inherent systematic uncertainty arising from the various correction procedures, approximately 5% for the 200GeV Au+Au collisions studied in this analysis. This uncertainty is referred to as the "scale" errors, due to the fact that it causes a uniform scaling effect to all points of the correlation function. In addition, since vertex position is a critical determinant of detector acceptance, the bin-by-bin systematic uncertainty caused by vertex position variation is studied by constructing correlation functions for 10 different vertex positions with other parameters fixed, obtaining the fluctuation of correlation function values for each bin, and quoting 1.6 $\times$ RMS as the 90% confidence level. This contribution amounted to approximately 6% over all bins.

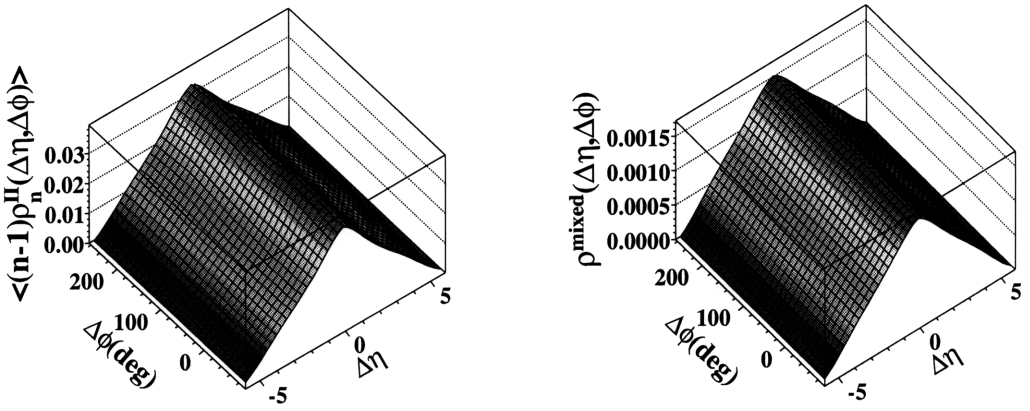

(a) Signal, PYTHIA

(b) Mixed-Event Background, PYTHIA

Figure 4.3: (a) Signal and (b) Background ($\Delta\eta$,$\Delta\phi$) distributions from PYTHIA

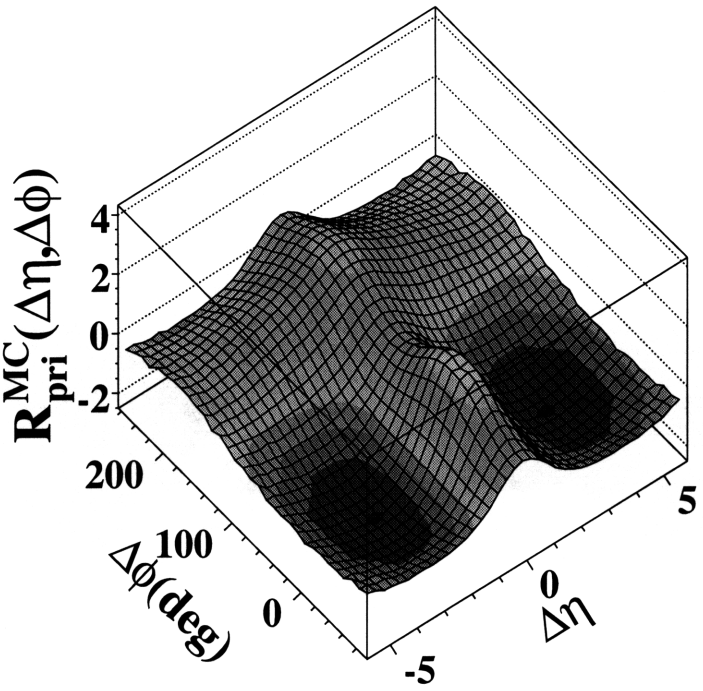

Figure 4.4: Two-particle correlation function constructed from (a) and (b).

4.4 Decomposition of the Correlation Function

The ultimate goal of this analysis is to decompose a two-particle correlation function into different components and observe their behavior with respect to changing centrality. In order to extract the contributing components of a correlation function, this paper chooses to fit the correlation function with the sum of expected components and analyze the change in fit parameters over a wide range of centralities. Each component is related with a functional form, and the sum of these functions build the fit function for the correlation function.

4.4.1 Fit Function Definition

In Fig. 4.5, a correlation function drawn from real data is compared to the corresponding fit function. This fit function is defined as below:

$$\begin{aligned} F(\Delta\eta, \Delta\phi) &= A_1 \cos(\Delta\phi) + A_2(\Delta\eta)\cos(2\Delta\phi) + A_3 e^{-\sqrt{(\Delta\eta/\sigma_{3,\Delta\eta})^2+(\Delta\phi/\sigma_{3,\Delta\phi})^2}} \\ &\quad + A_4 e^{-\Delta\eta^2/2\sigma_4^2} + A_5 e^{-(\Delta\eta^2/2\sigma_{5,\Delta\eta}^2+\Delta\phi^2/2\sigma_{5,\Delta\phi}^2)} + A_0. \end{aligned} \tag{4.7}$$

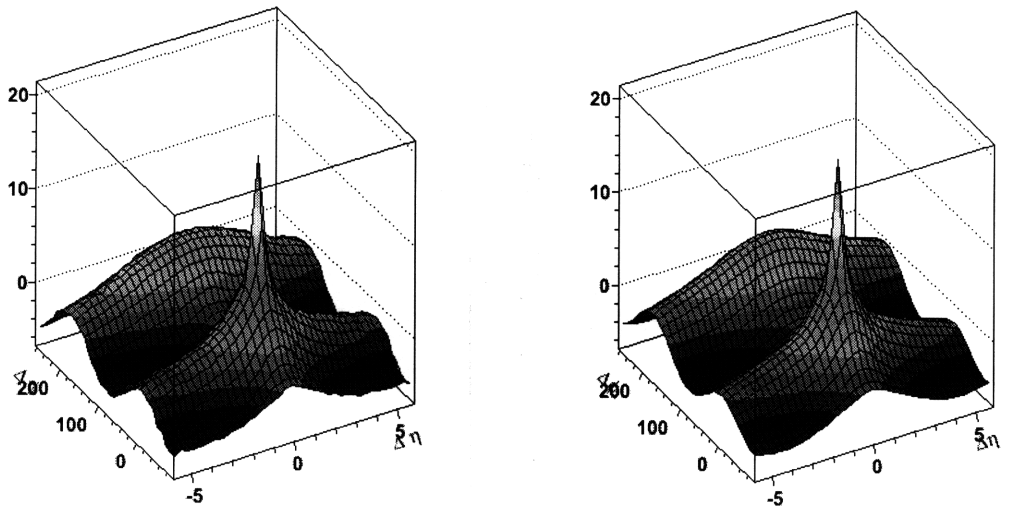

(a) (b)

Figure 4.5: A typical correlation function drawn from (a) data and the corresponding fit function (b).

4.4.2 Fit Function Structure

The previously discussed fit function contains six terms in total: level, $\cos(\Delta\phi)$, $\cos(2\Delta\phi)$, 1-D Gaussian, 2-D Gaussian, 2-D exponential peak. Figure 4.6 show the general shape of these terms except for the level term, which has no structure.

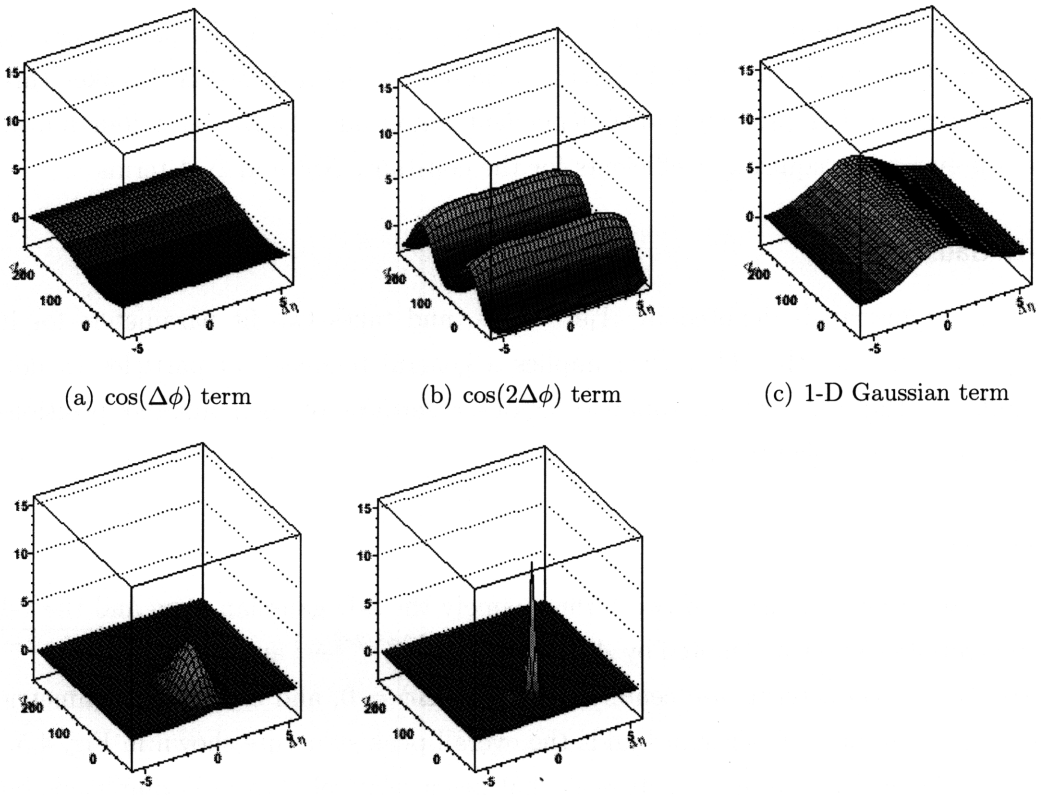

(a) $\cos(\Delta\phi)$ term (b) $\cos(2\Delta\phi)$ term (c) 1-D Gaussian term

(d) 2-D Gaussian term (e) Exponential peak term

Figure 4.6: General shapes of the (a) $\cos(\Delta\phi)$, (b) $\cos(2\Delta\phi)$, (c) 1-D Gaussian, (d) 2-D Gaussian, (e) exponential peak terms.

Level Term

The level term is denoted by A_0 in the fit function. It provides a uniform offset to the fit function, by raising or lowering the "level" of the baseline upon which other structures are built. Under ideal conditions, the level term would be vanish. The existence of a level term implies a discrepancy in correlation function normalization.

Angular Fluctuation Terms

The angular fluctuation terms constitute of two terms, namely the $\cos(\Delta\phi)$ term and the $\cos(2\Delta\phi)$ term. Angular correlations are usually analyzed in its Fourier decomposed form, and these two terms are the first and second order terms of the decomposition - terms of orders greater than two are neglected due to the insignificance of their contribution to the overall correlation function.

The $\cos(\Delta\phi)$ term is denoted by $A_1\cos(\Delta\phi)$ and takes one fit parameter, A_1. On the other hand, the $\cos(2\Delta\phi)$ term, denoted by $A_2(\Delta\eta)\cos(2\Delta\phi)$, takes three parameters, as the pseudorapidity-dependent amplitude $A_2(\Delta\eta)$ is a fourth-order even polynomial requiring coefficients for the constant, $\Delta\eta^2$ and $\Delta\eta^4$ terms.

1-D Gaussian

The 1-D gaussian is denoted by $A_4 e^{-\Delta\eta^2/2\sigma_4^2}$, and takes two fit parameters for its amplitude and width. This term implies a general tendency of particles to flock together within close pseudorapidity regions regardless of their angular positions, e.g. in clustering phenomena.

Peak Terms

The peak terms constitute of two terms, namely the 2-D gaussian term and the 2-D exponential peak term, denoted by $A_5 e^{-(\Delta\eta^2/2\sigma_{5,\Delta\eta}^2+\Delta\phi^2/2\sigma_{5,\Delta\phi}^2)}$ and $A_3 e^{-\sqrt{(\Delta\eta/\sigma_{3,\Delta\eta})^2+(\Delta\phi/\sigma_{3,\Delta\phi})^2}}$, respectively. Both terms are centered at $\Delta\eta = \Delta\phi = 0$, and exhibits a symmetric, peak-like structure. Their sum builds the overall peak structure shown in Fig. 4.5.

The 2-D gaussian term is a soft peak that has a relatively low peak amplitude but a larger peak area. This term represents a jet-like behavior of the particles to gather not only in pseudrapidity but also in the azimuthal angle, although much weaker and more frequent than real jets. This phenomenon is commonly known as the minijet phenomenon.

On the other hand, the exponential peak has a relatively high peak amplitude but is only significant in regions very close to $\Delta\eta = \Delta\phi = 0$. This term is not of an interest in terms of this analysis, as it arises mainly from detector effects such as the HBT effect. The HBT effect causes one particle to incur two hits on detectors very close to each other, which would result in a peak in correlation function just like the exponential peak. The HBT effect is discussed with more detail in Appendix ??.

5 Results and Physics Discussion

This chapter presents the final results drawn from the 200GeVAu+Au collision data using the aforementioned analysis methods. The calculated correlated function for centrality bins 3 through 15 are first presented, and the corresponding fit results are discussed. Also, a discussion of the robustness and physical implications of the fit results is given.

5.1 Correlation Function Results

Figure 5.1 shows the correlation functions calculated according to the methods described in Sect. 4.2. Centrality bins 3 through 15 were used in this analysis, due to the fact that the most peripheral and the most central data were not yet prepared with the appropriate corrections and calibrations. The correlation functions were imported into ROOT TH2 format, with 81 $\Delta\eta$ bins and 32 $\Delta\phi$ bins. The number of $\Delta\eta$ bins were chosen to be odd so that the peak center at $\Delta\eta = 0$ may be properly represented. One of the $\Delta\phi$ bins was centered at $\Delta\phi = 0$ for the same reason.

Examining Fig. 5.1 shows a gradual evolution of structures with respect to increasing centrality. While correlation functions within distance of one or two centrality bins are relatively similar to each other, note that central and peripheral correlation functions exhibit significant different structures.

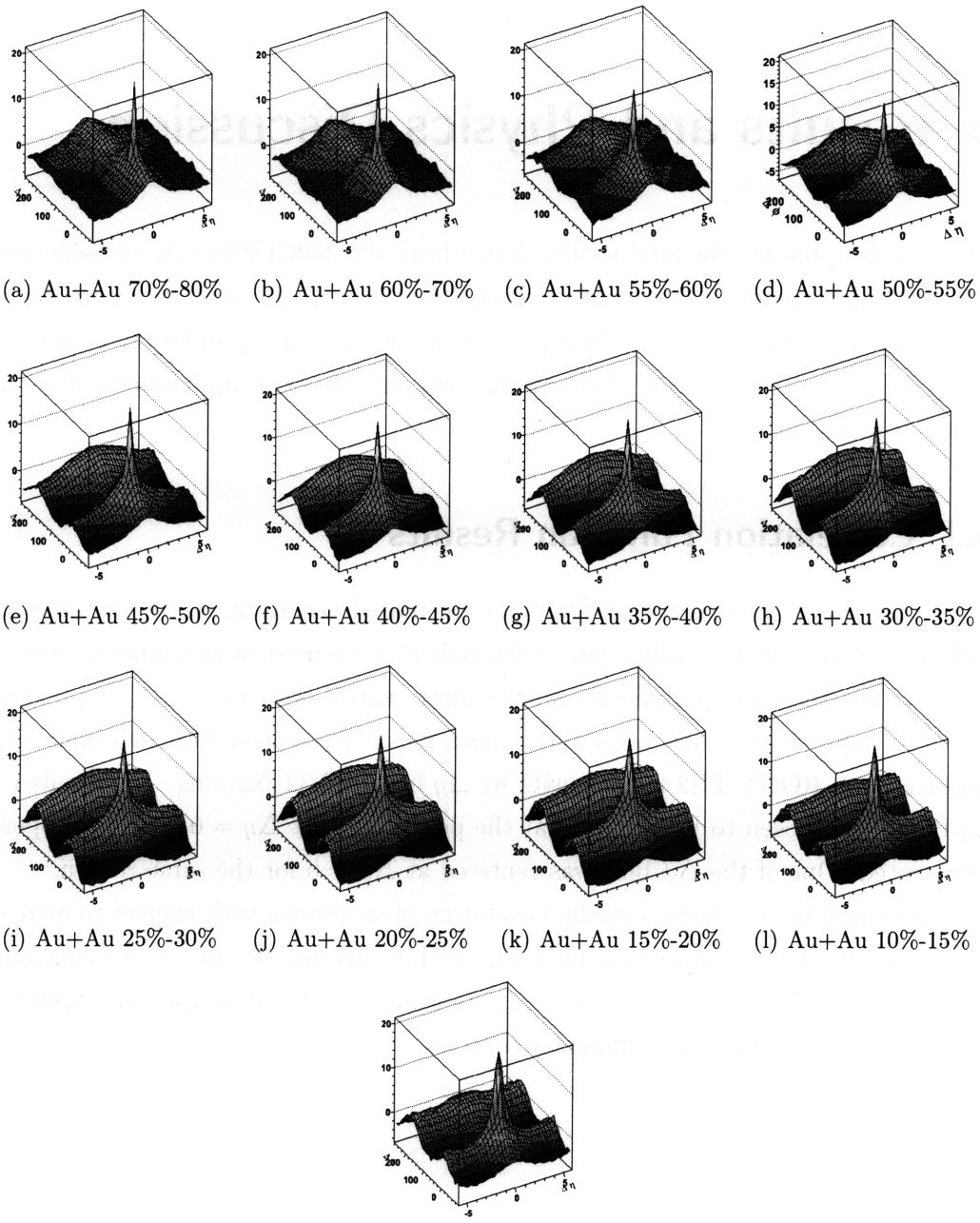

(a) Au+Au 70%-80% (b) Au+Au 60%-70% (c) Au+Au 55%-60% (d) Au+Au 50%-55%

(e) Au+Au 45%-50% (f) Au+Au 40%-45% (g) Au+Au 35%-40% (h) Au+Au 30%-35%

(i) Au+Au 25%-30% (j) Au+Au 20%-25% (k) Au+Au 15%-20% (l) Au+Au 10%-15%

(m) Au+Au 6%-10%

Figure 5.1: Two-particle correlation functions in the $(\Delta\eta - \Delta\phi)$ space for Au+Au collisions at $\sqrt{s_{\mathrm{NN}}} = 200\mathrm{GeV}$ for centrality bins 3 to 15.

5.2 Decomposition Results

The correlation functions obtained above were then fit with the fit functions defined in Sect. 4.4. The fitting procedures were carried out by ROOT, where a TF2 class was defined to reproduce the fit function and then fit to the 2-D histograms of correlation functions. A crucial element in making these fits work was to give initial values that closely resemble the data, as slight deviations, especially in the peak region, often lead the fit to end up completely different from the correlation function. However, as observed above, correlation functions of different centralities possess significantly different structure characteristics, and one set of initial values could not guarantee successful fits for all centralities. Therefore, several sets of initial values for small groups of centralities were first established by trial-and-error, and the actual fitting process started by taking its initial values from the initial value set corresponding to the correlation function being fitted.

Figure 5.2 exhibits the behavior of all 13 fit parameters with respect to changing N_{part}, a centrality variable. χ^2/dof values typically ranged from 0.2 to 0.4, and never exceeded 0.52. Notice that the overall behavior does not contain any sharp transitions or anomalous behavior at a certain point. It was noted in Sect. 1.4 that previous results [4] suggested a rapid transition of component behavior around the mid-centrality regime. More specifically, those results exhibited a rapid transition in angular fluctuation amplitude and 2-D Gaussian peak widths at $N_{\text{part}} \approx 50$, as discussed in Sect. 5.4. However, the behavior observed in the analysis of this paper contradicts those results.

Figure 5.3 and Fig. 5.4 shows the fit function and the residual (data-fit) for all correlation functions analyzed. A noticeable feature in the residuals is that as centrality increases, a $\cos(3\Delta\phi)$, or v3, structure slowly emerges. This tendency is the most visible for the most central correlation function, i.e. for the 6%-10% centrality bin. This is an expected result, as we have only taken v1 and v2 components into account. For low-centrality, and therefore low-multiplicity, events, the contribution of v3 is so low that it is dominated by other random fluctuations. However, as multiplicity increases with centrality, the contribution of v3 is large enough to be observed.

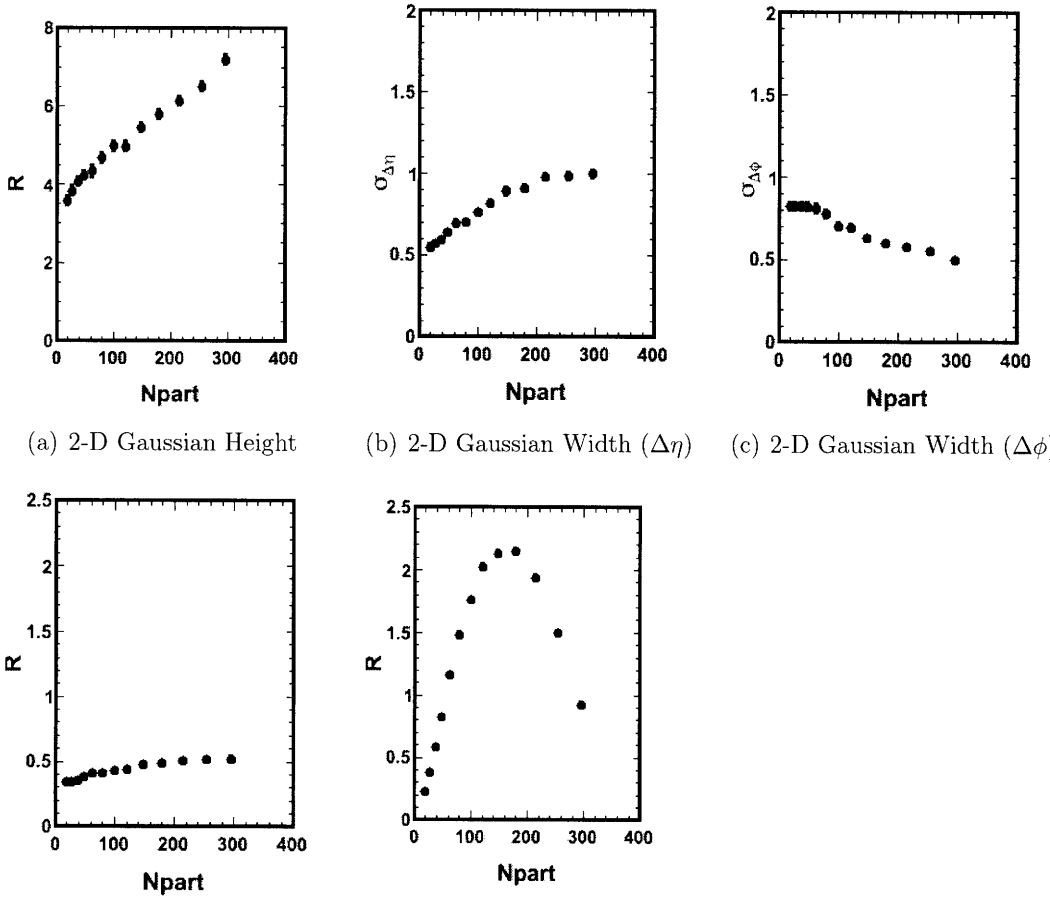

(a) 2-D Gaussian Height (b) 2-D Gaussian Width ($\Delta\eta$) (c) 2-D Gaussian Width ($\Delta\phi$)

(d) v1 component (e) v2 component

Figure 5.2: Fit results for fit parameters of 2-D Gaussian, v1 and v2 components.

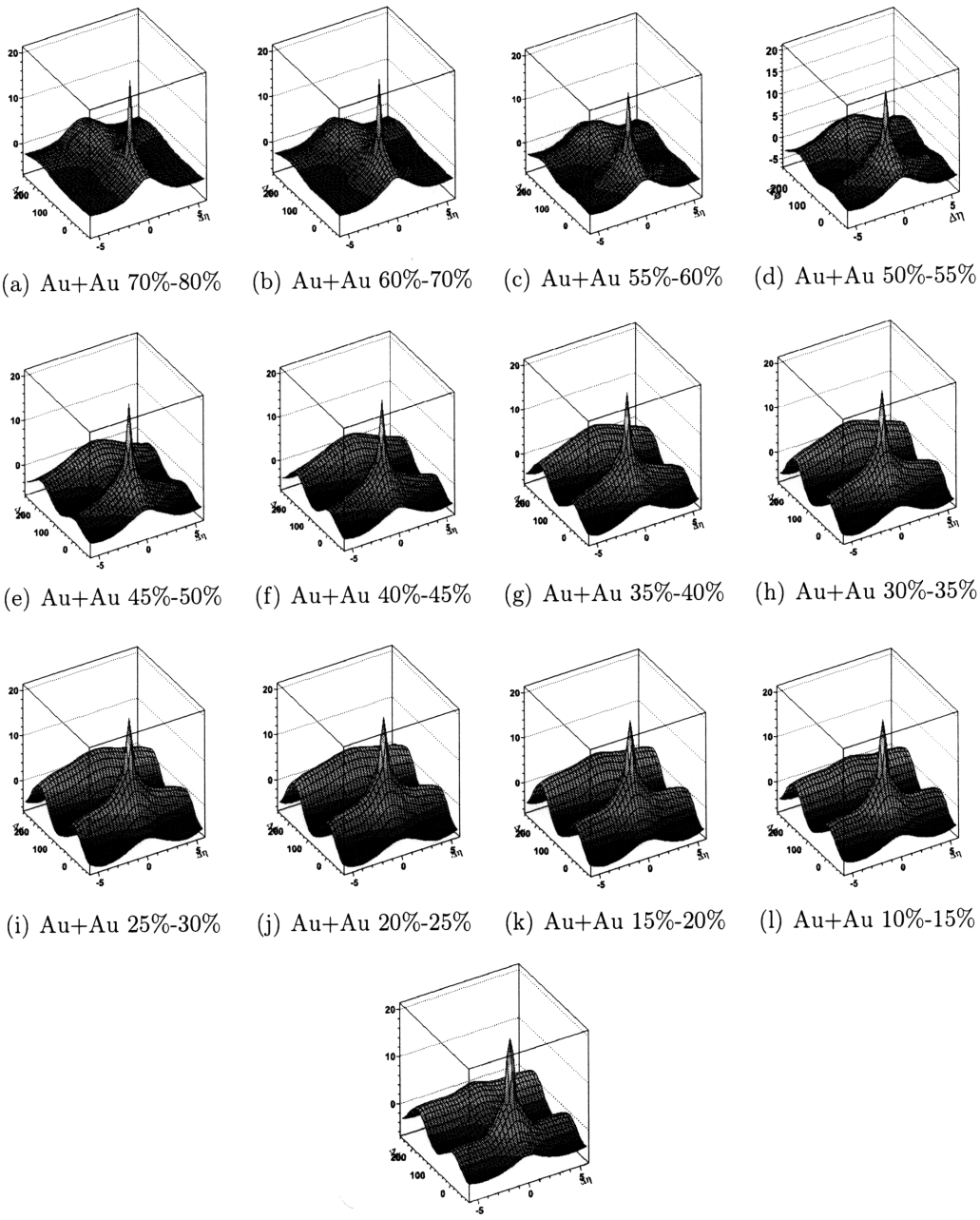

(a) Au+Au 70%-80% (b) Au+Au 60%-70% (c) Au+Au 55%-60% (d) Au+Au 50%-55%

(e) Au+Au 45%-50% (f) Au+Au 40%-45% (g) Au+Au 35%-40% (h) Au+Au 30%-35%

(i) Au+Au 25%-30% (j) Au+Au 20%-25% (k) Au+Au 15%-20% (l) Au+Au 10%-15%

(m) Au+Au 6%-10%

Figure 5.3: Fit functions for the calculated correlation functions in Fig. 5.1.

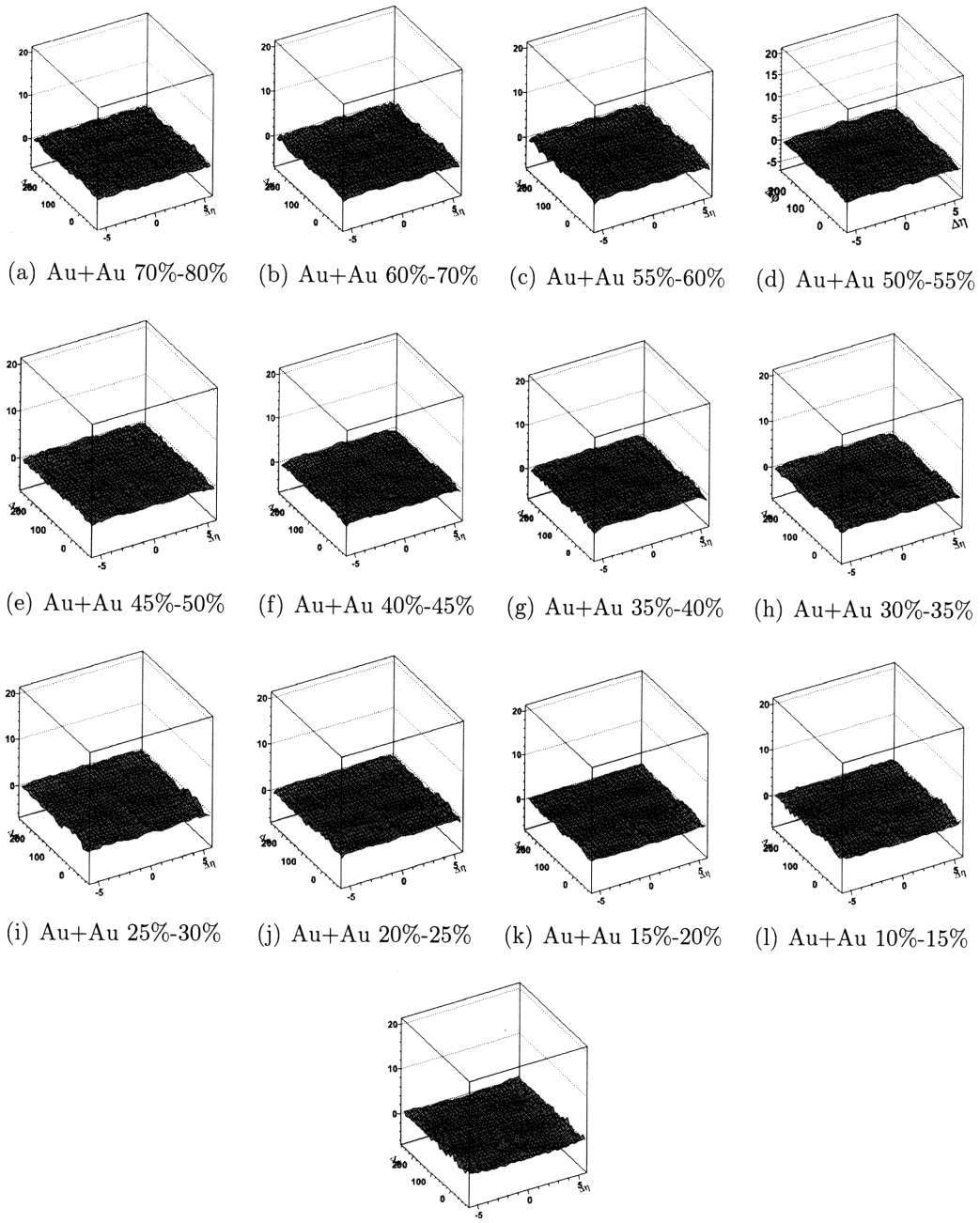

(a) Au+Au 70%-80% (b) Au+Au 60%-70% (c) Au+Au 55%-60% (d) Au+Au 50%-55%

(e) Au+Au 45%-50% (f) Au+Au 40%-45% (g) Au+Au 35%-40% (h) Au+Au 30%-35%

(i) Au+Au 25%-30% (j) Au+Au 20%-25% (k) Au+Au 15%-20% (l) Au+Au 10%-15%

(m) Au+Au 6%-10%

Figure 5.4: Fit residuals for the calculated correlation functions in Fig. 5.1.

5.3 Fit Degeneracy Analysis

A major issue raised to the method of decomposing correlation functions by fitting was the possibility of fit degeneracy, i.e. the possibility that two significantly different sets of fit parameters will yield equally satisfactory fit results. This is a possible scenario for the case of this analysis as well. For example, as the v1 component gives a positive contribution to the near side, a lower peak height may be compensated by a larger v1 component. The same scenario is possible with the level component and the peak height, or even between the level component and the v1 component. Other scenarios are improbable in that all other components are significantly localized, and therefore are unable to be compensated by any other component without significantly degrading the quality of the fits.

In order to test for the degeneracies between the three discussed variables, i.e. 2-D gaussian (minijet) peak height, v1 and level, the χ^2/dof distribution of fits with parameters close to the exact fit results was examined. Since calculating the χ^2/dof requires a full fit procedure, this could not be done in a continuous manner. Thus, each variable was given a set of possible values that are centered around the exact fit result and separated by small, uniform intervals, and a three-dimensional χ^2/dof distribution was calculated for all possible combinations of these possible values.

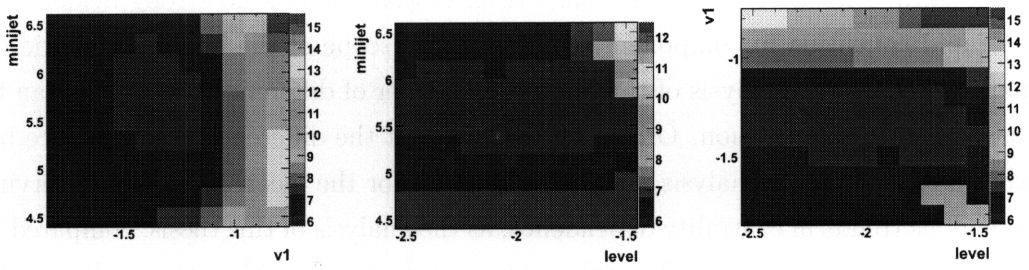

(a) Minijet height versus v1 component (b) Minijet height versus level component (c) v1 component versus level component

Figure 5.5: χ^2/dof distribution projected to (a)(v1-minijet height), (b)(level-minijet height), (c)(level-v1) spaces.

The above Fig. 5.5 shows the three projected 2-D χ^2/dof distributions. Existence of a degeneracy, implying a correlation or an anticorrelation between two variables, would appear as a diagonal contour, or, in the case of randomly occurring degeneracies, multiple localized spots. In the case of no degeneracies, an elliptical region, with its longer axis along the axis of the variable with less significance to the fit and its

shorter axis along that with more significance to the fit, will appear. Fig. 5.5 clearly exhibits that for no combination of variables the possibility of degeneracy exists, since all three distributions show elliptical contours without outliers. This confirms that the fit results of this analysis is robust with respect to fit degeneracy issues.

5.4 Concluding Remarks

5.4.1 Discussion of Physics Results

To draw comparison between the results of this thesis and the results of the STAR analysis, STAR results for components best exhibiting the anomalous trend in centrality dependence are shown in Fig. 5.6 along with the corresponding results from Fig. 5.3. The STAR results are plotted with variables of component amplitude and centrality different from this analysis. The difference in amplitude is largely a scale effect, as the STAR analysis employs a different definition of the correlation function $R(\Delta\eta, \Delta\phi)$. The centrality variable ν is defined as $\nu = 2 < N_{bin} > / < N_{\text{part}} >$, and is monotonically dependent on N_{part}. It was studied that the STAR results, when translated in terms of variables used in this analysis, will still exhibit its anomalous trends with little aberration.

The clear conclusion from this comparison is that there is no strong evidence of any rapid transition in component strength in the scope of the larger kinematic region covered by the analysis of this thesis. A number of different implications can be drawn from this conclusion. One implication is that the difference in acceptance between STAR and this analysis may be responsible for the inconsistency in observing anomalous trends in centrality dependence, as the analysis of this thesis, compared to the STAR analysis, takes significantly more particles over a wider range of kinematic region into account. It may be possible that the limited scope of the STAR analysis induces incorrect fit results that would not match with data when extrapolated out to a larger scope. Also, it may be the case where the anomalous trend is a localized phenomenon for particles with low transverse momentum, visible to the STAR analysis but diluted out in the analysis of this thesis.

All in all, the results of this analysis suggests that in the larger kinematic region of $|\Delta\eta| < 3$, no anomalous trends can be found. It seems that further attempts at similar analyses of experimental data will lead to successful and consistent results when it is accompanied by a satisfactory theoretical background. For example, there

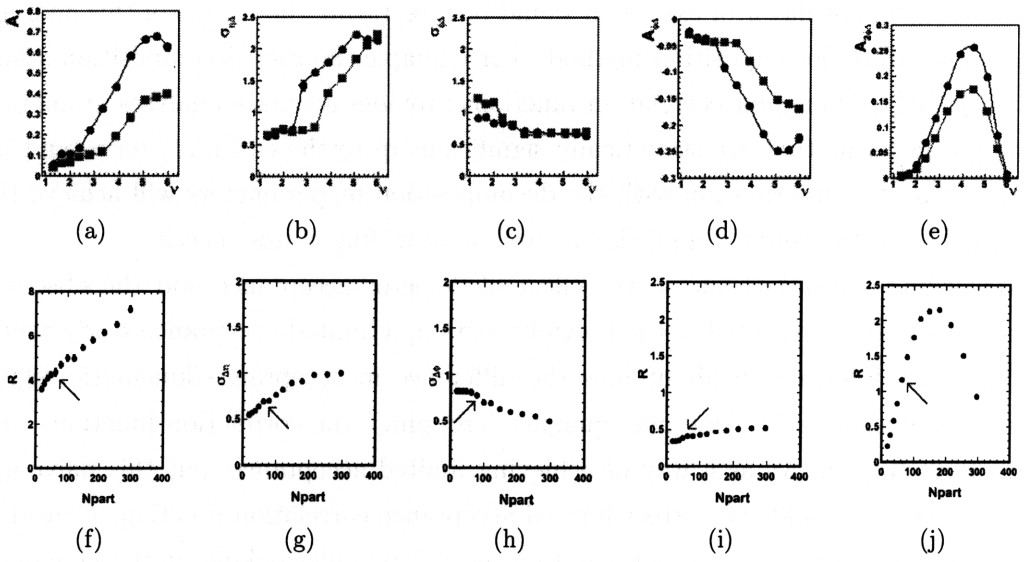

Figure 5.6: Comparison of the STAR results (upper five) with the results of this thesis (lower five). The plots are arranged in the following order: 2-D Gaussian height, 2-D Gaussian $\Delta\eta$ width, 2-D Gaussian $\Delta\phi$ width, v1 component, v2 component. The arrows placed in the lower five plots point to the expected point of anomalous behavior.

are numerous different theories explaining the minijet phenomenon, which accounts for the 2-D gaussian component in this analysis. However no one theory dominantly effective over others have emerged. A similar story is true for clustering phenomena, which corresponds to the 1-D gaussian component. With the development of successful theoretical descriptions of these contributing phenomena, the analysis of experimental data may obtain an additional degree of efficiency by exploiting the theoretical predictions as its starting point. As an example, a prediction on whether the minijet phenomena are localized to the low-pseudorapidty regime would greatly clarify the inconsistency between the two analyses discussed above.

5.4.2 Possible Extensions

The analysis of this paper can be extended with several different studies. A trivial extension would be to extend the range of covered centralities to the whole centrality domain, i.e. including centrality bins 1, 2 and 16 through 18. Another extension similar to this would be an extrapolation of obtained results with MC simulations. Since PHOBOS data agrees amazingly well with HIJING, the results of this analysis may be extended to a much wider region through appropriate MC tuning proce-

dures. A different flavor of extension would be integrating the results of this analysis with a separate decomposition method. For example, Fourier decomposition study of projected 1-D angular correlation functions provides accurate analyses of angular fluctuation terms that are statistically significant up to the $\cos(4\Delta\phi)$ term, and incorporating this information with the decomposition fit parameters will achieve the twin goal of establishing a guideline as well as providing a cross-check.

Regarding the discussion on the effect of detector acceptance and the observed kinematic region presented in the previous section, a limited-acceptance study would reveal more information about how the difference in acceptance/kinematic region affects analysis results. One may imagine "cropping" the correlation functions to a narrower range in $\Delta\eta$ as a way of achieving limited acceptance, but this naive approach does not yield the correct limited-acceptance correlation function. Consider, for example, limiting our acceptance to $|\Delta\eta| < 2$ by only looking at the kinematic region $|\eta| < 1$. If we simply cut our existing correlation function, particles from $\eta = 2$ and $\eta = 3$ will fit inside a $|\Delta\eta| < 1$ cut, but these particles are both outside of the targeted acceptance range. Rather, the correlation functions must be calculated again with a different set of constraints. This limited-acceptance study will also make the comparison between the results of this analysis and those of the STAR analysis more intuitive.

A PHOBOS Collaboration List

B. Alver[4], B. B. Back[1], M. D. Baker[2], M. Ballintijn[4], D. S. Barton[2], R. R. Betts[6], R. Bindel[7], W. Busza[4], Z. Chai[2], V. Chetluru[6], E. García[6], T. Gburek[3], K. Gulbrandsen[4], J. Hamblen[8], I. Harnarine[6], C. Henderson[4], D. J. Hofman[6], R. S. Hollis[6], R. Hołyński[3], B. Holzman[2], A. Iordanova[6], J. L. Kane[4], P. Kulinich[4], C. M. Kuo[5], W. Li[4], W. T. Lin[5], C. Loizides[4], S. Manly[8], A. C. Mignerey[7], R. Nouicer[2], A. Olszewski[3], R. Pak[2], C. Reed[4], E. Richardson[7], C. Roland[4], G. Roland[4], J. Sagerer[6], I. Sedykh[2], C. E. Smith[6], M. A. Stankiewicz[2], P. Steinberg[2], G. S. F. Stephans[4], A. Sukhanov[2], A. Szostak[2], M. B. Tonjes[7], A. Trzupek[3], G. J. van Nieuwenhuizen[4], S. S. Vaurynovich[4], R. Verdier[4], G. I. Veres[4], P. Walters[8], E. Wenger[4], D. Willhelm[7], F. L. H. Wolfs[8], B. Wosiek[3], K. Woźniak[3], S. Wyngaardt[2], B. Wysłouch[4]

[1] Argonne National Laboratory, Argonne, IL 60439-4843, USA
[2] Brookhaven National Laboratory, Upton, NY 11973-5000, USA
[3] Institute of Nuclear Physics PAN, Kraków, Poland
[4] Massachusetts Institute of Technology, Cambridge, MA 02139-4307, USA
[5] National Central University, Chung-Li, Taiwan
[6] University of Illinois at Chicago, Chicago, IL 60607-7059, USA
[7] University of Maryland, College Park, MD 20742, USA
[8] University of Rochester, Rochester, NY 14627, USA

B Kinematic Variables

In high-energy physics, the longitudinal axis is parametrized in terms of rapidity variable, y:

$$\begin{aligned} y &= \frac{1}{2}\ln\left(\frac{E+p_z}{E-p_z}\right). \\ &= \frac{1}{2}\ln\left(\frac{1+\beta}{1-\beta}\right). \end{aligned} \tag{B.1}$$

The rapidity variable is additive under Lorentz transformation. In this sense, rapidity in relativistic mechanics is analogous to velocity in non-relativistic mechanics. Expanding y in Eq. B.1 with respect to β gives:

$$y = \beta + O(\beta^3). \tag{B.2}$$

Therefore, for $\beta << 1$ rapidity is essentially a measure of velocity.

It is convenient to approximate rapidity with pseudorapidity which can be determined based only on the polar angle θ. This is is a good approximation in the high-energy limit where the particle mass is small compared to its momentum.

$$\begin{aligned} y &= \frac{1}{2}\ln\left(\frac{E+p_z}{E-p_z}\right) \\ &\approx \frac{1}{2}\ln\left(\frac{p+p_z}{p-p_z}\right) \qquad \text{for } m^2 \ll E^2 \\ &= \frac{1}{2}\ln\left(\frac{p+p\cos(\theta)}{p-p\cos(\theta)}\right) \\ &= \frac{1}{2}\ln\left(\frac{1+\cos(\theta)}{\sin(\theta)}\,\frac{\sin(\theta)}{1-\cos(\theta)}\right) \\ &= \frac{1}{2}\ln\left(\frac{1}{\tan(\theta/2)}\,\frac{1}{\tan(\theta/2)}\right) \end{aligned} \tag{B.3}$$

$$y \approx -\ln\left(\tan(\theta/2)\right) \equiv \eta \tag{B.4}$$

For a particle of rest mass m_0 and transverse momentum transverse p_{T} , a transverse mass of the particle can be define: $m_T = \sqrt{m_0^2 + p_{\mathrm{T}}^2}$. This gives rise to the following useful relations:

$$E = m_T \cosh(y). \tag{B.5}$$

$$p = p_{\mathrm{T}} \cosh(y). \tag{B.6}$$

$$p_z = m_T \sinh(y). \tag{B.7}$$

C Glauber Model

The *Glauber model* describes multiple collision processes at the baryon level, assuming that the colliding nucleon can still be approximated as a baryon-like object which make further collisions along the direction of incidence without deflection under the same baryon-baryon cross section (see Fig. C.1).

N_{part} measures the total number of nucleons participating inside a collision event. However, since each goes through more than one collision in a collision event, a new variable N_{coll} is defined to be the number of binary collisions. The Glabuer model gives a context in which a relationship between N_{part} and N_{coll} can be formulated (see Fig. C.2). In this model, each nucleus consisted of nucleons randomly arranged according to a "Woods-Saxon" probability distribution:

$$\rho(r) = \frac{\rho_0}{1 + \exp\left(\frac{r-R}{d}\right)} \tag{C.1}$$

where $\rho(r)$ is the normalized nuclear density, R (6.5 fm for Au) is the nuclear radius, and d (0.54 fm for Au) is the surface thickness. The total inelastic p+p cross section measured from the data is used, which has 42 ± 1 mb at 200 GeV and 36 ± 1 mb at 62.4 GeV.

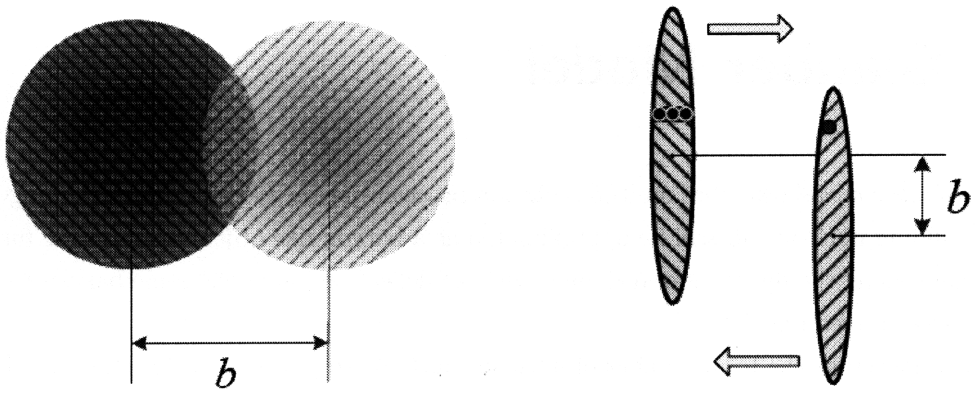

(a) View down the beam (b) Side view

Figure C.1: Geometric illustration of an collision event with impact parameter b. (a) View along the beam and (b) from the side [22].

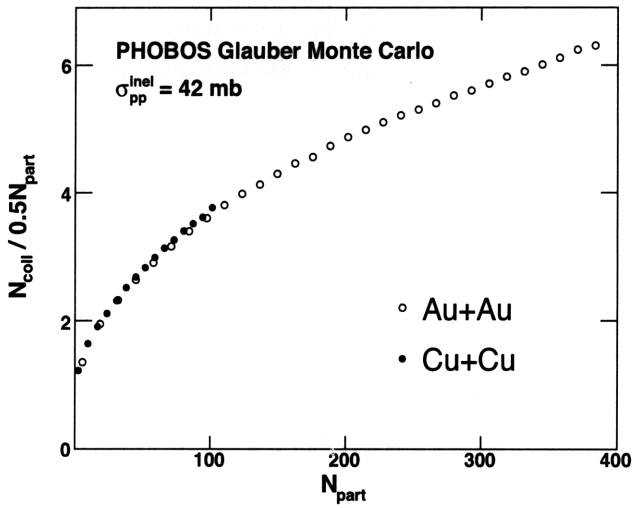

Figure C.2: The total number of binary collisions N_{coll} per participating nucleon pair for Cu+Cu and Au+Au from Glauber Model [18].

D Centrality Tables

Bin	Fraction	PdlMean Cuts	N_{part}	N_{coll}
17	0% to 3%	1889.7 to 99999.0	359 ± 10.6	1105 ± 79.2
16	3% to 6%	1722.3 to 1889.7	330 ± 10.7	984 ± 73.0
15	6% to 10%	1519.0 to 1722.3	297 ± 9.8	847 ± 63.2
14	10% to 15%	1290.3 to 1519.0	256 ± 8.2	685 ± 50.5
13	15% to 20%	1085.3 to 1290.3	215 ± 6.8	537 ± 39.5
12	20% to 25%	902.8 to 1085.3	181 ± 6.3	421 ± 32.0
11	25% to 30%	743.4 to 902.8	149 ± 6.2	321 ± 26.4
10	30% to 35%	603.0 to 743.4	123 ± 6.3	245 ± 22.6
9	35% to 40%	483.4 to 603.0	101 ± 6.3	186 ± 19.5
8	40% to 45%	377.8 to 483.4	82.1 ± 6.2	138 ± 16.7
7	45% to 50%	288.5 to 377.8	64.9 ± 5.8	99.1 ± 13.7

Table D.1: Centrality selections used in Au+Au collisions at $\sqrt{s_{\text{NN}}} = 200$ GeV. The PdlMean cuts were `TrgCuts_PR04_200_BP` and `TrgCuts_PR04_200_BM`.

E List of Acronyms

Facilities:

AGS	Alternating Gradient Synchrotron (http://www.bnl.gov/bnlweb/facilities/AGS.asp)
BNL	Brookhaven National Laboratory (http://www.bnl.gov/)
CERN	European Organization for Nuclear Research – *Conseil Européen pour la Recherche Nucléaire* (http://public.web.cern.ch/public/)
LHC	Large Hadron Collider (http://lhc.web.cern.ch/lhc/)
RHIC	Relativistic Heavy Ion Collider (http://www.bnl.gov/RHIC/)

Physics Terminology:

HIJING	Heavy Ion Jet Interaction Generator (http://www-nsdth.lbl.gov/ xnwang/hijing/)
QCD	Quantum Chromodynamics
QGP	Quark Gluon Plasma

PHOBOS and RHIC Hardware:

ADC	Analog-to-Digital Converter
DAC	Digital-to-Analog Converter
DAQ	Data Acquisition
DMU	Data Multiplexing Unit
FEC	Front-End Controller
FPDP	Front Panel Data Port

E List of Acronyms

HPSS	High Performance Storage System (http://www.hpss-collaboration.org/hpss/index.jsp)
PhAT	PHOBOS Analysis Toolkit
RCF	RHIC Computing Facility
SpecTrig	Spectrometer Trigger
TAM	Tree-Analysis Modules
TOF	Time-of-Flight
T0	Time-Zero Counter
VME	VERSAmodule Eurocard
ZDC	Zero-Degree Calorimeter

Experimental Terminology:

CMN	Common-Mode Noise
MC	Monte Carlo
MinBias	Minimum Bias
NSD	Non-Sigle-Diffractive
PdlMean	Paddle Mean
PdlTDiff	Paddle Time Difference

Bibliography

[1] S Chakrabarty. On the possibility of nuclear liquid-gas phase transition. *Journal of Physics G: Nuclear and Particle Physics*, 20(3):469–475, 1994. URL `http://stacks.iop.org/0954-3899/20/469`.

[2] J. C. Collins and M. J. Perry. Superdense matter: Neutrons or asymptotically free quarks? *Phys. Rev. Lett.*, 34(21):1353–1356, May 1975.

[3] Edward Shuryak. Quantum chromodynamics and the theory of superdense matter. *Physics Reports*, 61(2):71–158, 1980.

[4] Michael Daugherity. Angular Correlations in STAR. *PoSCFRNC*, 2006:005, 2006.

[5] M. Harrison, T. Ludlam, and S. Ozaki. RHIC project overview. *Nucl. Instrum. Meth.*, A499:235–244, 2003.

[6] M. Harrison, Stephen G. Peggs, and T. Roser. The RHIC accelerator. *Ann. Rev. Nucl. Part. Sci.*, 52:425–469, 2002.

[7] K. H. Ackermann et al. STAR detector overview. *Nucl. Instrum. Meth.*, A499: 624–632, 2003.

[8] K. Adcox et al. PHENIX detector overview. *Nucl. Instrum. Meth.*, A499:469–479, 2003.

[9] M. Adamczyk et al. The BRAHMS experiment at RHIC. *Nucl. Instrum. Meth.*, A499:437–468, 2003.

[10] B. B. Back et al. The PHOBOS detector at RHIC. *Nucl. Instrum. Meth.*, A499: 603–623, 2003.

[11] C. Henderson. *Identified Particle Transverse Momentum Distributions from Au+Au Collisions at 62.4 GeV per Nucleon Pair.* PhD thesis, Massachusetts Institute of Technology, 2005.

[12] R. Bindel, E. García, A. C. Mignerey, and L. P. Remsberg. Array of scintillator counters for PHOBOS at RHIC. *Nucl. Instrum. Meth.*, A474:38–45, 2001.

[13] B.G. Gibbard and T.G. Throwe. The rhic computing facility. *Nucl. Instr. Meth.*, A499:814–818, 2003.

[14] R. Brun and F. Rademakers. Root. *Nucl. Instr. Meth.*, A389:81, 1997.

[15] R. Nouicer et al. Silicon pad detectors for the PHOBOS experiment at RHIC. *Nucl. Instrum. Meth.*, A461:143–149, 2001. [arXiv:nucl-ex/0208006].

[16] M. Plesko, J. Fitch, D. Ross, C. Gomes, P. Kulinich, H. Pernegger, P. Sarin, and B. Wadsowrth. Front-end electronics for the silicon partition of the phobos detector at rhic. *Nuclear Science Symposium Conference Record, 2001 IEEE*, 1: 76–80 vol.1, Nov. 2001. ISSN 1082-3654.

[17] A. Sukhanov, P. Kulinich, and P. Sarin. A gigabit/s data acquisition system. *rtc*, 0:123, 2005.

[18] E. Wenger. *Studies of High Transverse Momentum Phenomena in Heavy Ion Collisions Using the PHOBOS Detector.* PhD thesis, Massachusetts Institute of Technology, 2008.

[19] R. Hollis. *Centrality Evolution of Charged Particles Produced in Ultra-relativistic Au+Au and d+Au Collisions.* PhD thesis, University of Illinois at Chicago, 2005.

[20] Michael L. Miller, Klaus Reygers, Stephen J. Sanders, and Peter Steinberg. Glauber modeling in high energy nuclear collisions. *Ann. Rev. Nucl. Part. Sci.*, 57:205–243, 2007.

[21] K. Eggert et al. Angular Correlations Between the Charged Particles Produced in p p Collisions at ISR Energies. *Nucl. Phys.*, B86:201, 1975.

[22] W. Li. *Clustering Phenomena from Two-particle Angular Correlations in Proton-Proton and Heavy Ion Collisions.* PhD thesis, Massachusetts Institute of Technology, 2009.

List of Figures

List of Tables

Acknowledgments

As this thesis concludes my undergraduate studies of physics, it becomes evident this thesis, and the past four years that led me to this thesis, would not have been possible without the support and guidance I received from numerous individuals. I owe more thanks to them than what can be written in words, but I will attempt to express as much of it as possible.

First of all, I would like to show my sincere gratitude to Professor Gunther Roland, my thesis advisor and also my UROP advisor of two years. I first met him in my sophomore summer while cluelessly searching for a UROP position, and ever since then he has always guided me towards valuable lessons and opportunities. He not only gave me research projects to work on or opportunities to work at CERN, but also made sure that I was approaching physics with the correct attitude in mind. His legacy on how one should carry out physics research will remain with me forever. Also, I would like to extend my thanks to Professor Wit Busza and Professor Bolek Wyslouch. Wit has always been an inspiring figure, constantly stimulating the students around him to investigate the fundamentals and to look at the big picture. Bolek always played an important role in the group with his leadership, while maintaining a constant interest in my research endeavors.

Speaking of professors, I am deeply indebted to Professor John Belcher, my academic advisor. John has helped me getting through the hardest time of my undergraduate career with kind advices at each and every step I would take. His mentorship has been the crucial element in refreshing myself with a new passion for physics, and I will be forever grateful to him for the interest and support he has always shown to me.

For the last two years, I was honored to work with the members of the MIT Heavy Ion Group. My officemates, Burak Alver, Wei Li and Siarhei Varuynovich, have been wonderful mentors and colleagues. I learned almost every single bit of heavy ion physics from Burak, and this thesis would not have been possible without the sturdy foundation established by Wei and Burak. They have been always good to me, way

more than what I deserve, and I sincerely thank them for it. I would also like to mention the CERN crew of the group; Yen-Jie Lee, Frank Ma, Yetkin Yilmaz, Andre Yoon and Yongsun Kim. With them I have spend an amazing summer, tasting CERN to the fullest and gaining invaluable experiences. Arya Tafvizi, my fellow UROP student at CERN, has always been a close friend of mine since the day we first inside the CERN group meeting. I express my gratitude for his friendship, and also for the amazing parties at his fraternity.

Lastly, and perhaps most importantly, I would like to thank my family. Nothing, and by this I mean truly nothing, would have been possible wIthout the selfless love and support from my parents, No-Ho Park and Hyunsook Kim. The sacrifices they have made for me are unimaginably large and many, as I have left their side at a very young age to pursue my dream of studying science. I am always grateful for the fact that they have always encouraged me to study what I had a passion for. I am afraid I will never be a good son for them, but they have always been the best I could imagine. I love you.